

Journal Pre-proofs

Sulfate sulfur isotopes and major ion chemistry reveal that pyrite oxidation counteracts CO₂ drawdown from silicate weathering in the Langtang-Trisuli-Narayani River system, Nepal Himalaya

P.C. Kemeny, G.I. Lopez, N.F. Dalleska, M. Torres, A. Burke, M.P. Bhatt, A.J. West, J. Hartmann, J.F. Adkins

PII: S0016-7037(20)30684-0
DOI: <https://doi.org/10.1016/j.gca.2020.11.009>
Reference: GCA 11984

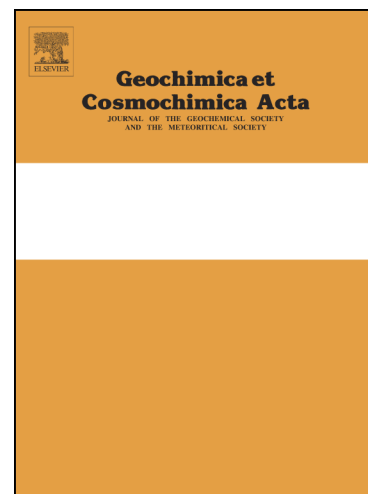
To appear in: *Geochimica et Cosmochimica Acta*

Received Date: 14 April 2020
Revised Date: 2 November 2020
Accepted Date: 11 November 2020

Please cite this article as: Kemeny, P.C., Lopez, G.I., Dalleska, N.F., Torres, M., Burke, A., Bhatt, M.P., West, A.J., Hartmann, J., Adkins, J.F., Sulfate sulfur isotopes and major ion chemistry reveal that pyrite oxidation counteracts CO₂ drawdown from silicate weathering in the Langtang-Trisuli-Narayani River system, Nepal Himalaya, *Geochimica et Cosmochimica Acta* (2020), doi: <https://doi.org/10.1016/j.gca.2020.11.009>

This is a PDF file of an article that has undergone enhancements after acceptance, such as the addition of a cover page and metadata, and formatting for readability, but it is not yet the definitive version of record. This version will undergo additional copyediting, typesetting and review before it is published in its final form, but we are providing this version to give early visibility of the article. Please note that, during the production process, errors may be discovered which could affect the content, and all legal disclaimers that apply to the journal pertain.

© 2020 Elsevier Ltd. All rights reserved.



Sulfate sulfur isotopes and major ion chemistry reveal that pyrite oxidation counteracts CO₂ drawdown from silicate weathering in the Langtang-Trisuli-Narayani River system, Nepal Himalaya

P.C. Kemeny^{a*}, G.I. Lopez^a, N. F. Dalleska^a, M. Torres^b, A. Burke^c, M.P. Bhatt^d, A.J. West^e, J. Hartmann^f, J.F. Adkins^a

^a Division of Geological and Planetary Sciences, California Institute of Technology, Pasadena, California, USA

^b Department of Earth, Environmental, and Planetary Sciences, Rice University, Houston, Texas

^c School of Earth and Environmental Sciences, University of St Andrews, St Andrews, UK

^d Department of Physical and Environmental Sciences, Concord University, Athens, WV, USA

^e Department of Earth Science, University of Southern California, Los Angeles, California, USA

^f Institute for Geology, Universität Hamburg, Bundesstrasse, Hamburg, Germany

*Corresponding author: pkemeny@caltech.edu

Highlights:

- $\delta^{34}\text{S}_{\text{SO}_4}$ and major ions are set by lithology principally and seasonality secondarily
- Sulfide and S_{org} oxidation source 62-101% of SO_4^{2-} in Langtang-Trisuli-Narayani
- The fraction of H_2SO_4 -driven weathering varies seasonally with system hydrology
- Narayani catchment weathering does not reduce pCO_2 on timescales >5 Kyr and <10 Myr

Abstract:

Drawdown of atmospheric carbon dioxide (CO₂) due to silicate weathering in the Himalaya has previously been implicated in Cenozoic cooling. However, over timescales shorter than that of the removal of marine sulfate (SO₄²⁻), the oxidation of pyrite (FeS₂) in weathering systems can counteract the alkalinity flux of silicate weathering and modulate pCO₂. Here we present evidence from sulfur isotope ratios in dissolved SO₄²⁻ ($\delta^{34}\text{S}_{\text{SO}_4}$), together with dissolved major ion concentrations, that reveals FeS₂ oxidation throughout the Langtang-Trisuli-Narayani River system of the Nepal Himalaya. River water samples were collected monthly to bi-monthly throughout 2011 from 16 sites ranging from the Lirung Glacier catchment through the Narayani River floodplain. This sampling transect begins in the High Himalayan Crystalline (HHC) formation and passes through the Lesser Himalayan (LH) formation with upstream influences from the Tethyn Sedimentary Series (TSS). Average $\delta^{34}\text{S}_{\text{SO}_4}$ in the Lirung Glacier outlet is 3.6‰, increases downstream to 6.3‰ near the confluence with the Bhote Kosi, and finally declines to -2.6‰ in the lower sites. Using new measurements of major ion concentrations, inversion shows 62-101% of river SO₄²⁻ is derived from the oxidation of sulfide minerals and/or organic sulfur, with the former process likely dominant. The fraction of H₂SO₄-driven weathering is seasonally variable and lower during the monsoon season, attributable to seasonal changes in the relative influence of shallow and deep flow paths with distinct residence times. Inversion results indicate that the primary control on $\delta^{34}\text{S}_{\text{SO}_4}$ is lithologically variable isotope composition, with the expressed $\delta^{34}\text{S}$ value for the LH and TSS formations (median values -7.0‰ to 0.0‰ in 80% of samples) lower than that in the HHC (median values 1.7‰ to 6.2‰ in 80% of samples). Overall, our inversion indicates that FeS₂ oxidation counteracts much of the alkalinity flux from silicate weathering throughout the Narayani River system such that weathering along the sampled transect exerts minimal impact on pCO₂ over timescales >5 -10 Kyr and <10 Myr. Moreover, reanalysis of prior datasets suggests that our findings are applicable more widely across several of the frontal Himalayan drainages.

1. Introduction

Chemical weathering exerts a first-order influence on climate by regulating the flux of dissolved inorganic carbon (DIC) and alkalinity (ALK) delivered from the terrestrial surface into the ocean-atmosphere system (Walker et al., 1981; Gaillardet et al., 1999). Previously, silicate weathering of the Himalaya has been implicated in the long-term cooling of the Cenozoic (Raymo et al., 1988; Raymo & Ruddiman, 1992; Zachos et al., 2001). The associated “uplift-weathering” hypothesis has inspired extensive debate on the nature and controls of silicate weathering, both in the Himalaya and globally, with a particular emphasis on interpreting the Cenozoic rise in marine $^{87}\text{Sr}/^{86}\text{Sr}$ (Elderfield, 1986; Veizer, 1989; Edmond, 1992; Krishnaswami & Singh, 1998; Krishnaswami et al., 1999; Myrow et al., 2015). The controls on chemical weathering have been traditionally posed as a dichotomy between physical processes like uplift and erosion (Raymo & Ruddiman, 1992; Huh et al., 1998; Riebe et al., 2001; Millot et al., 2002) versus climate mechanisms related to temperature and the hydrologic cycle (Walker et al., 1981; White & Blum, 1995; Dessert et al., 2003). The debate has now shifted to reflect the continuum between physical and chemical controls as reflected in kinetically-limited weathering regimes and transport-limited or supply-limited weathering regimes (Stallard & Edmond, 1983; West et al., 2005; Maher & Chamberlain, 2014; Hilton & West, 2020). The Himalaya has continued to feature prominently in this discussion due to its varied lithology, topography, and potential role in Cenozoic cooling.

The role of the Himalaya in modulating Cenozoic atmospheric carbon dioxide (CO_2) levels remains an open question in part because the flux of silicate alkalinity from the major Himalayan rivers is relatively minor in the global context (France-Lanord & Derry, 1997; Galy & France-Lanord, 1999). This seemingly modest flux raises basic questions about whether Himalayan

silicate weathering could have driven Cenozoic $p\text{CO}_2$ decline. At the same time, without compensatory feedbacks, even modest increases in silicate weathering fluxes caused by Himalayan uplift could have quickly removed all CO_2 from the ocean-atmosphere system (Berner & Caldeira, 1997; Kerrick & Caldeira, 1999). To counteract such an over-drawdown of $p\text{CO}_2$, prior work has invoked a coincident flux of negative alkalinity through pyrite (FeS_2) oxidation (Torres et al., 2014), synorogenic metamorphic decarbonation (Bickle, 1996; Becker et al., 2008; Evans et al., 2008), a decrease in the magnitude of silicate weathering elsewhere (François & Walker, 1992; Kump & Arthur, 1997; Li & Elderfield, 2013), a decrease in burial of organic carbon (C_{org}) (Raymo, 1994), an increase in oxidation of petrogenic C_{org} (Beck et al., 1995), an increase in the subduction of pelagic carbonate sediments (Caldeira, 1992), or an increase in the formation of authigenic aluminosilicate minerals (Raymo & Ruddiman, 1992). This article explores the feasibility of the first hypothesis, that of sulfide mineral oxidation, through measurements of the sulfur isotope ratio of dissolved sulfate (SO_4^{2-}) and the concentrations of dissolved major ions in river water from the Langtang-Trisuli-Narayani River system in the Nepal Himalaya.

Previous research on chemical weathering of the Himalaya has focused primarily on the alkalinity flux from weathering of silicate minerals. This focus follows from the canonical framework of chemical weathering as the titration of carbonic acid (H_2CO_3) on silicate minerals (approximated as CaSiO_3) to generate alkalinity (eq. 1), which is subsequently consumed during formation and burial of marine carbonate mineral (CaCO_3) (eq. 2) (Urey, 1952). By removing one mole DIC from the ocean-atmosphere system for each mole of Ca^{2+} transferred from CaSiO_3 to CaCO_3 , the chemical weathering of silicates is often described as regulating atmospheric $p\text{CO}_2$ over geologic timescales (Sundquist, 1991). Within this same framework, the ALK and DIC sourced from

weathering of carbonate minerals (eq. 4) are consumed during burial of marine carbonate rock. Weathering of carbonate has thus traditionally been thought to have no net impact on atmospheric $p\text{CO}_2$ over timescales longer than the 5-10 Kyr timescale of marine carbonate compensation (Archer et al., 1997; 2000). Because the Nepal Himalaya is dominated by carbonate weathering (Blum et al., 1998; Galy & France-Lanord, 1999), prior studies argued that the dominant influence of Himalayan weathering on the geologic carbon cycle relates to organic carbon burial (France-Lanord & Derry, 1997; Galy et al., 2007) or metamorphic carbon fluxes (Bickle, 1996; Becker et al., 2008; Evans et al., 2008).



The canonical weathering framework outlined above ignores sources of H^+ other than DIC, yet the oxidation of sulfide minerals can also provide H^+ that impact the global carbon cycle (Spence & Telmer, 2005; Lerman et al., 2007; Calmels et al., 2007) (eq. 5). The oxidation of minerals such as FeS_2 generates sulfuric acid (H_2SO_4) that rapidly deprotonates to SO_4^{2-} , removing both ALK and dioxygen (O_2) from the ocean-atmosphere system. The oxidation of FeS_2 can also proceed through reduction of Fe^{3+} to Fe^{2+} (eq. 6) (Balci et al., 2007) with significantly greater consumption of ALK per mole of released SO_4^{2-} . However, aerobic re-oxidization of Fe^{2+} results in the net reaction being equivalent to that of direct O_2 reduction (eq. 5). Alkalinity lost through FeS_2 oxidation is ultimately returned to the ocean-atmosphere system over the timescale for SO_4^{2-} to be

removed from the ocean in marine sediments through reduction to FeS₂; the residence time of SO₄²⁻ in the modern ocean is approximately 10 Myr (Burke et al., 2018). The impacts of FeS₂ oxidation on pCO₂ are thus manifest during the period over which FeS₂-derived SO₄²⁻ accumulates in seawater. Although a role for sulfide oxidation was recognized early in major river systems (Rabinovich & Grinenko, 1979; Stallard & Edmond, 1983), including in the Himalaya (Galy & France-Lanord, 1999), FeS₂ oxidation as a globally-relevant sink of alkalinity has only recently been appreciated (Torres et al., 2014; Burke et al., 2018).



More broadly, any source of SO₄²⁻ entering the ocean-atmosphere system without charge compensation by conservative cations removes ALK. For example, the oxidation of organo-sulfate moieties to SO₄²⁻ and DIC consumes 2 moles ALK per mole SO₄²⁻, the same stoichiometry as FeS₂ oxidation (eq. 5). When considering the role of sulfur as a source of H⁺ for weathering, what matters is thus the provision of SO₄²⁻ without the addition of conservative cations, rather than the oxidation of sulfide within any particular mineral phase. The relative importance of sulfide mineral oxidation versus the oxidation of modern or rock-bound organic sulfur (S_{org}) depends on factors such as the relative abundance of S-bearing phases, the availability of oxidants, and the presence of relevant microbial communities. However, because most S in typical siliciclastic sedimentary rocks is as sulfide minerals and not S_{org}, it is reasonable to assume that the majority of non-evaporite SO₄²⁻ liberated from rocks during weathering derives from FeS₂-oxidation. Here we thus combine all sources of SO₄²⁻ without cation release under the umbrella term of “FeS₂ oxidation”

and note that this includes SO_4^{2-} sourced to the river through oxidation of reduced carbon, as well as the oxidation of additional sulfide minerals where the partner cation remains in the solid phase.

Although reactions releasing SO_4^{2-} without compensating cations have similar effects on ALK, they can have different implications for DIC and thus for pCO_2 ; sources of SO_4^{2-} associated with S-C bonds will typically increase ocean-atmosphere DIC upon oxidation, while sources of SO_4^{2-} from inorganic minerals are unlikely to directly impact DIC. By not resolving the DIC fluxes associated with oxidation and production of organic matter, our work thus provides only a partial view of the full influence of chemical weathering on atmospheric pCO_2 (Hilton & West, 2020). Furthermore, we do not consider the nitrogen or cation fluxes associated with biomass growth and oxidation, which may counteract or reinforce the ALK dynamics of SO_4^{2-} addition to river water. Over geologic timescales, the different sources of SO_4^{2-} may also have distinct implications for pO_2 . Estimates of the full balance of organic and inorganic weathering are only available for a few settings globally (Horan et al., 2019; Hilton & West, 2020), and the Nepal Himalaya is a natural choice for future research quantifying dissolved rhenium in river water (Hilton et al., 2014).

Oxidation of mineral-bound sulfide and organic sulfur in the Himalaya thus represent additional and understudied levers on the carbon cycle, with particular relevance for understanding Cenozoic pCO_2 decline. In their pioneering work, Galy & France-Lanord (1999) proposed that 70% of SO_4^{2-} in samples from the Narayani River system of the Nepal Himalaya derived from FeS_2 oxidation. Using measurements of DIC $^{13}\text{C}/^{12}\text{C}$ from the same study, Torres et al. (2014) proposed that sulfide oxidation in the Ganges-Brahmaputra fully counteracts the ALK flux of silicate weathering and potentially helped to sustain pCO_2 at moderate levels throughout the Cenozoic. Any increase in

pCO₂ from with sulfide oxidation could have significantly offset drawdown from increases in silicate weathering, land surface reactivity, or Cenozoic C_{org} storage (France-Lanord & Derry, 1997), or accentuated increases in synorogenic decarbonation (Bickle, 1996; Becker et al., 2008).

Analogous to silicate weathering, FeS₂ oxidation in the Himalaya has both physical and climatic controls. Foremost, lithology controls the abundance of available sulfide minerals and thus the ability of those lithologies to generate sulfuric acid. Moreover, FeS₂ cannot be transported more than a few km through O₂-rich environments without oxidation (Johnson et al., 2014). As a corollary, sulfide oxidation is thought to almost always be supply-limited, suggesting a strong erosional control on FeS₂ oxidation and thus a gradient across geomorphic setting (Calmels et al., 2007). Oxidation of FeS₂ may also be influenced by runoff and temperature (Brantley et al., 2013), convolving H₂SO₄ into the seasonal weathering cycle; for example, if seasonal variations in hydrology control the depth of penetration of oxidizing fluids (Winnick et al., 2017). Here we present evidence for seasonal changes in the fraction of H₂SO₄-driven weathering, complementing prior evidence from throughout the Himalaya for seasonality in carbonate weathering (Tipper et al., 2006).

Sulfur isotope ratios of dissolved riverine SO₄²⁻ ($\delta^{34}\text{S}_{\text{SO}_4} = {}^{34}\text{R}_{\text{sample}}/{}^{34}\text{R}_{\text{VCDT}} - 1$, commonly reported in ‰ relative to Vienna Canyon Diablo Troilite (VCDT) and where ³⁴R is the ³⁴S/³²S ratio of SO₄²⁻) are a useful tool for studying FeS₂ oxidation. Previously, $\delta^{34}\text{S}_{\text{SO}_4}$ was measured in the Marsyandi River of the Nepal Himalaya (Turchyn et al., 2013; Hemingway et al., 2020). Because the studied region of the Marsyandi represents only a relatively small fraction of the total Narayani catchment, the Nepal Himalaya remains largely uncharacterized for $\delta^{34}\text{S}_{\text{SO}_4}$.

In this article we report the dissolved major ion chemistry and $\delta^{34}\text{S}_{\text{SO}_4}$ of seasonal river water samples from throughout the Langtang-Trisuli-Narayani River system (Fig. 1) in order to test the impacts of lithology and seasonality on FeS_2 oxidation. Using a Monte Carlo inversion model, we show that the Narayani catchment hosts significant FeS_2 oxidation. We find that $\delta^{34}\text{S}_{\text{SO}_4}$ is principally set by lithology and identify seasonal changes in the fraction of H_2SO_4 -driven weathering. Over timescales less than approximately 10 Myr, the ALK flux of sulfuric acid weathering may completely counteract the drawdown of pCO_2 due to silicate weathering in the Langtang-Trisuli-Narayani River system.

2. Methods

2.1. Field methods and sample context

2.1.1. Sample collection

The samples analyzed in this study are river waters from the Langtang-Trisuli-Narayani River system in central Nepal (Fig. 1a), previously presented in Bhatt et al. (2018). Briefly, samples were collected monthly or bimonthly throughout 2011 at 16 sites (LNS-1 through LNS-16) ranging in elevation from 169 m to 3989 m (Fig. 1b). During collection each sample was filtered through a $0.45\ \mu\text{m}$ polycarbonate filter into a single 100 mL acid-washed polyethylene bottle (Bhatt et al., 2018). Samples were not acidified, but our testing did not reveal carbonate precipitation or sorption of ions to container walls (Appendix 1). These samples are an important resource for future studies on weathering in the Nepal Himalaya because they record conditions prior to the 2015 Gorkha earthquake and associated landsliding (Roback et al., 2018).

Prior to collection, sample bottles were washed with a mixture of KOH and Neodisher LaboClean A 8 (NaOH, Na₂CO₃, Na₂SiO₃*5H₂O, C₃Cl₂N₃NaO₃), cleaned with 2% HCl, rinsed with water and then several times with DI water, and dried in an oven. Overall, measurements of [Cl⁻] in our sample bottles are higher than prior measurements from the same river system (Appendix 1). Moreover, our data shows coherent variations in [K⁺] and [Cl⁻], which are two components of the cleaning solution. However, we do not believe that these observations reflect contamination of the samples through the cleaning protocol. The samples enriched in [Cl⁻] also tend to be elevated in other dissolved ions, showing coherent variability across ion systems that argues against significant Cl⁻ contamination. Likewise, the [Cl⁻] and [K⁺] variation is nearly independent of [Na⁺], another major component of the cleaning solution, and thus not suggestive of contamination from bottle washing as a major cause of chemical variability. The results and data analyses presented below include measurements of [K⁺], [Na⁺], and [Cl⁻], while calculations without [K⁺] and [Cl⁻] are presented as supplementary materials (Appendix D).

2.1.2. Sampling map and geologic context

The sampling transect begins in the Langtang River's headwaters in the Lirung Glacier catchment, passes through the confluence with the Bhoti Kosi to join the Trisuli River at Syabru Besi, and ends in the Narayani River after crossing confluences with the Budhi Gandaki, Marsyandi River, Seti River, and Kali Gandaki (Fig. 1b). Stations LNS-16 through LNS-7 are spaced progressively along the Langtang River. LNS-6 is on the Bhoti Kosi upstream of the confluence with the Langtang River, and LNS-5 is directly downstream of the confluence (Fig. 1c). For much of the year, the chemistry of samples from LNS-5 resembles that of LNS-6, suggesting a dominant influence from the western side of the confluence. Stations LNS-1 through LNS-4 sit on the Trisuli

and Narayani Rivers and are interspersed by major tributaries. The Budhi Gandaki enters the Narayani River between LNS-3 and LNS-2, and the Marsyandi River, Seti River, and Kali Gandaki enter between LNS-2 and LNS-1. The sites are thus broadly distinguishable into three subsets based on geographic distribution: stations LNS-1 to LNS-6 along the Trisuli-Narayani, stations LNS-7 to LNS-10 along the lower Langtang River, and stations LNS-11 to LNS-16 in the upper Langtang River as far upstream as the Lirung Glacier outlet.

The sampling transect passes through the major lithotectonic units of the Nepal Himalaya, including the High Himalayan Crystalline (HHC), the Lesser Himalayan (LH), the Siwaliks, and a portion of the floodplain (Fig. 1d). The HHC is a highly metamorphosed suite characterized by orthogneiss, paragneiss, migmatites, metapelite, and numerous leucogranite bodies (Galy & France-Lanord, 1999). The Main Central Thrust separates the HHC from the LH, and along this boundary are numerous hot springs (Bhattarai, 1980; Evans et al., 2001; 2004; 2008; Girault et al., 2014). The LH is composed of variably altered Precambrian metasediments including quartz-pelitic schist, massive dolomitic carbonates, and black shales (Pierson-Wickmann et al., 2000). The confluence of the Langtang River and the Bhote Kosi occurs at the boundary of the HHC with the LH, where hot springs are located at the town of Syabru Besi. Stations LNS-4 through LNS-2 are predominately within the LH formation, while LNS-1 sits below the Main Boundary Thrust on the floodplain built of detrital sediments.

The Tethyn Sedimentary Series (TSS) is exposed in the catchments of LNS-1 through LNS-6 and exerts a strong chemical influence on samples from these stations. The TSS is principally composed of the Phanerozoic marine shelf carbonates formed on the Indian margin prior to the

collision with Eurasia, and includes black shales (Wolff-Boenisch et al., 2009). No direct observations of halite or gypsum are reported for TSS in the Narayani catchment, although some work suggests its presence (Tshering & Bhandari, 1973 in Fort, 1996; Wolff-Boenisch et al., 2009; Appendix 2). The TSS was previously found to contain FeS_2 (Bordet et al., 1971) and FeS_2 oxidation is reported in the Marsyandi River (Turchyn et al., 2013; Hemingway et al., 2020), which is included in the headwaters of the catchment area captured by the most downstream sampling site in this study, LNS-1. The fraction of each catchment occupied by TSS decreases downstream from LNS-6, although the particular fraction depends on how much unmapped area is assigned to TSS. Here we assume 90% of the unmapped region for catchments LNS-2 through LNS-6 are composed of TSS, with the other 10% occupied by HHC, and that unmapped catchment area for LNS-1 is in proportion to the mapped fractions. Notably, our observations do not depend on these fractions; rather, the critical dynamic is simply that the catchments for LNS-1 through LNS-6 contain significant exposures of TSS and LH while the catchments for stations LNS-7 through LNS-16 contain much smaller exposures, if any.

2.1.3. Anthropogenic impacts on river chemistry

All samples were collected within 100 km of Kathmandu and a subset of samples were collected closer to urban centers such as Betrawati. The possibility for anthropogenic SO_4^{2-} contamination warrants particular attention given prior findings that approximately 30% of SO_4^{2-} in rivers globally is derived from anthropogenic pollution (Berner, 1971). Although the $\delta^{34}\text{S}$ of such pollution was previously thought to be low (Ivanov et al., 1983), recent research shows that polluted rivers can have a wide range of $\delta^{34}\text{S}_{\text{SO}_4}$ values (Burke et al., 2018). We account for the indirect input of anthropogenic SO_4^{2-} , such as through atmospheric transport of pollutants and

subsequent deposition, by using observations of precipitation chemistry in our analysis reflecting both natural and anthropogenic inputs. However, our analysis does not account for any direct inputs of SO_4^{2-} to the samples. If present, such pollution would lead us to overestimate the importance of FeS_2 oxidation. Although direct anthropogenic inputs are unlikely in the remote upstream sites above LNS-5, the potential for direct contamination increases downstream towards the urban centers of the floodplain; if present, anthropogenic inputs are expected to be largest at stations LNS-1 through LNS-4 (Fig. 1). Such a direct anthropogenic SO_4^{2-} source would likely result in a progressive downstream trend in $\delta^{34}\text{S}_{\text{SO}_4}$. Counter to this expectation, our data show that $\delta^{34}\text{S}_{\text{SO}_4}$ changes sharply at a lithologic boundary, which argues against a dominant role for the direct input of anthropogenic SO_4^{2-} . Although there are ultimately few constraints from river pH, $[\text{NH}_4^+]$, or $[\text{PO}_4^{3-}]$ with which to evaluate direct inputs from anthropogenic activities (Collins & Jenkins, 1996), the major ion chemistry of samples leads us to suspect sources of ions from pollution are minor relative to sources from chemical weathering (Appendix 2).

2.2. Experimental methods

2.2.1. Ion chromatography

The concentration of major cations and anions was measured by ion chromatography in the Environmental Analysis Center at the California Institute of Technology. The concentration of Ca^{2+} , Mg^{2+} , K^+ , and Na^+ was measured on a Dionex ICS-2000 equipped with a CG12A guard column (2 mm x 50 mm) and a CS12A separator column (2 mm x 250 mm) with an isocratic 20 mM methanesulfonic eluent. SO_4^{2-} and Cl^- concentrations were measured on a Dionex ISC-3000 equipped with an AG29 guard column (2 mm x 50 mm) and an AS29 separator column (2 mm x 250 mm) with an isocratic 4.5 mM / 2.5 mM Na_2CO_3 / NaHCO_3 eluent. All major ion

concentrations were measured with suppressed conductivity detection. The precision of IC measurements was typically better than 4% for samples (2σ , relative standard deviation) and always better than 11.6% (the least-reproducible ion in the least-reproducible solution, including reference solutions measured both before and after addition of HNO_3^-) but varied by element and solution (Appendix 1, Table S1). Bicarbonate (HCO_3^-) is calculated by charge balance for plotting purposes but is not included in our inversion model.

The concentration of major ions in these samples was previously measured in Hamburg and reported in Bhatt et al. (2018). During the course of this study we identified systematic differences between new measurements and the previously published values, with the discrepancy correlated to the month of sample collection (Appendix 1). In this analysis we use the new measurements of $[\text{Ca}^{2+}]$, $[\text{Mg}^{2+}]$, $[\text{Na}^+]$, $[\text{K}^+]$, $[\text{Cl}^-]$, and $[\text{SO}_4^{2-}]$ generated at Caltech.

2.2.2. MC-ICP-MS measurements of $\delta^{34}\text{S}_{\text{SO}_4}$

River samples were evaporated to dryness overnight in acid-washed Savillex containers, dissolved in dilute hydrochloric acid, and passed through anion-exchange resin (AG 1-X8 analytical grade 100-200 mesh chloride form) to isolate SO_4^{2-} , similar to the chromatography protocols of Paris et al. (2013) and Burke et al. (2018). The isolated SO_4^{2-} was then matrix-matched to an in-house Na_2SO_4 solution previously calibrated to international reference materials and $\delta^{34}\text{S}$ was measured by Multi-Collector Inductively-Coupled-Plasma-Mass-Spectrometry (MC-ICP-MS) with sample-standard bracketing (Paris et al., 2013). Measurement cycles were analyzed both visually and statistically to determine outliers and a post-run correction was applied to remove instrument blank and procedural blank. The analytical method typically included two attempts to measure each

eluate on a given run, and the observed differences between the two observations relative to their expected difference based on internal precision was quantified using Error-Normalized Deviation (END) (John & Adkins, 2010). After removal of samples with measurement artifacts such as rapid changes in mass biasing, the standard deviation of the internal END distribution over 10 runs ranged from 1.3 to 8.3.

The $\delta^{34}\text{S}_{\text{SO}_4}$ of IAPSO seawater was measured as $20.99 \pm 0.25\text{‰}$ ($n=53, 2\sigma$). The $\delta^{34}\text{S}_{\text{SO}_4}$ of Switzer Falls, a local river used as an internal reference material (Burke et al., 2018), was measured as $4.25 \pm 0.39\text{‰}$ ($n=53, 2\sigma$). All 121 river water samples were measured at least twice, and 48 samples were fully processed twice with a mean $\delta^{34}\text{S}$ difference of 0.20‰ between the two determinations. The reported error on each sample is taken to be the larger of either the standard deviation of blank-corrected $^{34}\text{S}/^{32}\text{S}$ ratios, or the reproducibility of references across all analytical sessions (taken to be $2\sigma = 0.40\text{‰}$).

2.3. Principal component analysis

Variation in the concentration of Ca^{2+} is responsible for much of the absolute variance among dissolved ions. To identify trends related to the location of sampling and season of collection, we subtract the mean and divide by the standard deviation (Z -score) of the major ion chemistry and $\delta^{34}\text{S}_{\text{SO}_4}$ measurements prior to performing principal component analysis (PCA) (Glover et al., 2011). Some prior work normalized dissolved ion concentrations by Na^+ prior to analysis, following an a-priori assumption of systematic changes due to seasonal dilution (Négrelet et al., 1993). Here we do not further normalize the Z -scored data, meaning that any trends related to seasonal decreases in solute concentrations will be reflected in the results of the PCA. We plot

factor loadings, which are the correlation coefficient of the Z-scored data with its projection into the basis of principal components (Negrel et al., 1993). We also plot normalized sample factor scores, which are a projection of the Z-scored data into the basis of principal components scaled by singular values and then normalized to the ratio of the maximum factor score to the maximum Euclidean distance of the plotted factor loadings.

2.4. Monte Carlo inversion model

2.4.1. Using solute chemistry to reconstruct weathering

At circumneutral pH, HCO_3^- dominates the anion budgets of many rivers and is the major reservoir of riverine DIC. As a result, the *in-situ* ALK/DIC ratio of many rivers is close to one. However, the parameter that ultimately impacts the long-term carbon cycle is the $\Delta\text{ALK}/\Delta\text{DIC}$ ratio of the overall weathering system sourcing ions to the river, which is different from the *in-situ* value of ALK/DIC measured in a river at any given point in space and time. Two reasons for this discrepancy are that rivers undergo gas exchange with the atmosphere (Striegl et al., 2012; Raymond et al., 2013), as well as exchange of CO_2 with the environment through aquatic respiration and photosynthesis (Quay et al., 1995). Due to this non-conservative behavior, *in-situ* $[\text{HCO}_3^-]$ reflects the integrated history of biological and physical processes within the river, in addition to chemical weathering. These processes may be important for understanding how in-river processes contribute to the global balance of photosynthesis and respiration, but do not reflect the weathering processes that regulate pCO_2 on geologic timescales. Simply measuring $[\text{HCO}_3^-]$ fails to account for the upstream fluxes that have continuously modified the *in-situ* values of ALK and DIC, and thus cannot be used to calculate the $\Delta\text{ALK}/\Delta\text{DIC}$ ratio of the overall weathering system.

Unlike $[\text{HCO}_3^-]$, dissolved major ions are largely conservative in most river systems and can be used to reconstruct the $\Delta\text{ALK}/\Delta\text{DIC}$ ratio of weathering. To do so for samples from the Langtang-Trisuli-Narayani River system, the contribution of distinct lithologies to the river dissolved load was calculated using a Monte-Carlo inversion model (Négrel et al., 1993; Gaillardet et al., 1999; Torres et al., 2016; Burke et al., 2018; Hemingway et al., 2020). This inversion is analogous to prior studies of river chemistry both globally (Gaillardet et al., 1999) and in the Himalaya specifically (Bickle et al., 2015), but differs from the forward-modeling common in some prior work in the region (Galy & France-Lanord, 1999; Tipper et al., 2006). We discuss the results of our full inversion model below and include as supplementary material a subset of analogous results for a forward model (Appendix 4) that uses seawater ratios for precipitation (Sarmiento & Gruber, 2006). We derive two parameters from inversion results previously introduced in Torres et al. (2016), R and Z, which respectively reflect the relative amount of silicate and carbonate weathering and the relative importance of CO_2 and H_2SO_4 as sources of H^+ . Because the $\Delta\text{ALK}/\Delta\text{DIC}$ of the weathering system is a simple function of the values of R and Z, our analysis focuses on their relative values as well as spatial and seasonal changes in the two parameters.

2.4.2. Inversion end-members

The inversion uses two carbonate end-members, two silicate end-members, and precipitation (Table 1). Motivating observations for our selections are given in Appendix 2, including comparison of our carbonate and silicate end-members with those used in prior work and our decision to exclude evaporite minerals and hot springs from our primary inversion; results including evaporites (Claypool et al., 1980; Valdiya, 1980; Sarin & Krishnaswami, 1984; Singh &

Singh, 2010) and hot springs (Evans et al., 2004) are given in Appendix 4. Guided by observations of downstream changes in Mg^{2+}/Σ^+ (where $\Sigma^+ = Ca^{2+} + Mg^{2+} + Na^+ + K^+$ in units of charge equivalents) we separate carbonate contributions into those from calcite and dolomite. We do not include Na^+ or K^+ in the carbonate end-members; this decision is enabled by the normalization to Σ^+ rather than Na^+ , which leaves the end-members free to be stoichiometric. Coherently changing K^+/Na^+ ratios motivates the use of two silicate end-members. The first end-member is called 'silicate' and is assigned a high Na^+/Σ^+ and low K^+/Σ^+ , while the second end-member is called 'biotite' and is assigned Na^+/Σ^+ and K^+/Σ^+ opposite to the silicate end-member (Table 1). The silicate end-member represents generic silicate weathering (e.g., feldspars, muscovite), while the biotite end-member represents a K^+ -rich phase which may be preferentially weathered during the monsoon season to increase K^+/Na^+ .

Most studies in the Himalaya have appealed to the existence of an end-member with a Cl^-/Na^+ ratio near 1. Galy & France-Lanord (1999) accounted for the Cl^- in excess of rainwater inputs using a $NaCl$ end-member, and subsequent work has often used a Cl^- -rich hot spring (Evans et al., 2004; Tipper et al., 2006) or seawater (Bhatt et al., 2018). The lack of evaporite minerals or high- Cl^-/Σ^+ hot springs along most of our sampling transect suggests that rainwater sources nearly 100% of Cl^- in our samples. As a result, the precipitation end-member is the only source of Cl^- in our primary inversion model. Changing this assumption impacts results for the fraction of carbonate weathering but exerts only minimal influence on the calculated fraction of H_2SO_4 -driven weathering (Appendix 4). The chemical ratios of the precipitation end-member are determined from observation (Handa, 1968; Sequeira & Kelkar, 1978; Galy & France-Lanord, 1999; Bhatt et

al., 2000; Shrestha et al., 2002; Hren et al., 2007; Andermann et al., 2011; Balestrini et al., 2014; Tripathy et al., 2014; Panthi et al., 2015) (Fig. S5).

Torres et al. (2016) and Burke et al. (2018) represent two different approaches to account for FeS₂ oxidation in river chemistry. In Torres et al. (2016), FeS₂ oxidation is included directly in the inversion by allowing silicate and carbonate end-members to have non-zero SO₄²⁻/Σ⁺ and well-defined δ³⁴S values. In Burke et al. (2018), FeS₂ oxidation is calculated post-inversion through SO₄²⁻ mass balance. Our analysis combines the SO₄²⁻/Σ⁺ approach of Torres et al. (2016) with the post-inversion calculation for the δ³⁴S of FeS₂ (δ³⁴S_{FeS2}) allowed in the approach of Burke et al. (2018). Following Torres et al. (2016), we take the SO₄²⁻/Σ⁺ ratio of the non-precipitation end-members to reflect H₂SO₄-driven weathering. Using the measured sample δ³⁴S_{SO4} and precipitation δ³⁴S_{SO4}, we then calculate by mass balance the δ³⁴S of the SO₄²⁻ sourced from the calcite, dolomite, silicate, and biotite end-members, which we take as the value of δ³⁴S_{FeS2}. Each river sample thus constrains a distribution of possible δ³⁴S_{FeS2} values. Note that these inversion-constrained values of δ³⁴S_{FeS2} reflect the net δ³⁴S of SO₄²⁻ delivered without conservative cations; that is, values of δ³⁴S_{FeS2} formally reflect SO₄²⁻ sourced from both sulfide mineral oxidation and S_{org} oxidation or accumulation, as opposed to the specific δ³⁴S of FeS₂ mineral.

2.4.3. Inversion methodology

On a given iteration, the Ca²⁺/Σ⁺, Na⁺/Σ⁺, K⁺/Σ⁺, and Cl⁻/Σ⁺ of each end-member were pulled randomly from normal distributions with end-member-specific means and standard deviations (Table 1). The ratio SO₄²⁻/Σ⁺ was pulled from a normal distribution for the precipitation end-member, where observations inform the expected range of values. Because there is little empirical

evidence for the fraction of H_2SO_4 -driven weathering associated with each lithology, the $\text{SO}_4^{2-}/\Sigma^+$ for each non-precipitation end-member was pulled from a uniform distribution between 0 and 1. All distributions were truncated with a lower bound of zero, and those with a numerator constituent to Σ^+ were truncated with an upper bound of 1. The ratios of Mg^{2+}/Σ^+ for each end-member were calculated to ensure mass balance based on the other cation ratios (although indicated in Table 1, the Mg^{2+}/Σ^+ distributions were not drawn directly). If a calculated Mg^{2+}/Σ^+ was negative, the entire process was repeated up to 500 times or until a set of physically realizable, mass balanced end-members was generated. On a given iteration the river data for $[\text{Ca}^{2+}]$, $[\text{Mg}^{2+}]$, $[\text{Na}^+]$, $[\text{K}^+]$, $[\text{Cl}^-]$, and $[\text{SO}_4^{2-}]$ were altered by values pulled randomly from a normal distribution with mean of zero and standard deviation corresponding to analytical precision (Appendix 1).

The resulting set of river observations and end-member chemistry was solved using the MATLAB function *fmincon*; the optimization cost function was the sum of squared proportional offsets between observations and model estimate, constrained to deliver positive solutions, and used as an initial condition the solution from standard least-squares inversion. Simulation results were not accepted if any variable was more than 15% discrepant from observations. One hundred thousand simulations were attempted; the first 1000 successful simulations for each sample were kept. All samples were successfully inverted 1000 times except the July and August sample at LNS-4 (0 successes) and the August sample at LNS-07 (233 successes). In most calculations we use the median of accepted simulation results and take the 5th and 95th percentiles of accepted simulation results as the inversion error. We note that the full range of results should be considered possible because the result of river inversions can be sensitive to the introduction of additional elemental or isotope systems (Torres et al., 2016).

2.4.4. Influence of secondary carbonate precipitation

Two assumptions of the Monte Carlo inversion are that the net solute release from each end-member is described by the range of chemical ratios we sample, and that these weathering products mix conservatively. However, evidence from dissolved chemistry (Jacobson et al., 2002), bedload chemistry (Bickle et al., 2015), and Ca^{2+} isotope ratios (Tipper et al., 2008) all indicate that there is secondary calcite precipitation in Himalayan rivers. Some evidence positively correlates the fraction of Ca^{2+} lost from solution with the strength of silicate weathering (Bickle et al., 2015), so that the impacts of secondary calcite formation are expected to be largest during the non-monsoon season (Tipper et al., 2006). Bickle et al. (2015) estimate the magnitude of Ca^{2+} remaining after secondary carbonate precipitation to be 5-40% in the TSS and 40-100% in the HHC. The range of the estimates derives mostly from the nature of the calculation and not from chemical variability.

Secondary carbonate precipitation biases the interpretation of which end-members are weathering but not which acids are responsible for weathering. The first impact of secondary calcite precipitation is to decrease observed Ca^{2+}/Σ^+ , causing inversions to underestimate the true fraction of carbonate weathering (Fig. S8). Assuming 50% of Ca^{2+} was removed as secondary carbonate precipitation in our HHC-dominated samples (Bickle et al., 2015), we calculate that the effect of secondary carbonate precipitation was to lower absolute Ca^{2+}/Σ^+ by ~10% (Fig. S8). Second, secondary carbonate precipitation will increase $\text{SO}_4^{2-}/\Sigma^+$ so that it does not reflect the fraction of gross weathering driven through sulfide oxidation. We again estimate the absolute magnitude of this effect to be ~10% (Fig. S8). Because the importance of secondary carbonate precipitation likely varies throughout the catchment, our calculations are only approximations. However,

because the formation of CaCO_3 produces H^+ , observed Σ^+ still remains a valid metric of net H^+ consumption during weathering. That is, even in the presence of secondary carbonate precipitation, the ratio $\text{SO}_4^{2-}/\Sigma^+$ reflects net sulfuric acid weathering. In detail, the shift in the relative fraction of carbonate and silicate weathering also biases the inversion-constrained ranges of end-member $\text{SO}_4^{2-}/\Sigma^+$ (Fig. S8). Because our analysis is primary concerned with variation in $\text{SO}_4^{2-}/\Sigma^+$, $\delta^{34}\text{S}_{\text{SO}_4}$, and the seasonality of FeS_2 oxidation, our findings are largely insulated against impacts from secondary carbonate precipitation. We do not correct our data for secondary carbonate precipitation.

2.5. Construction of a synthetic hydrograph

Three gauging stations along the sampling transect (Fig. 1, Q1-Q3) record similar annual hydrographs with elevated flow during the monsoon season and reduced flow during the non-monsoon (Fig. S7). Discharge at Q1 and Q3 during 2011 were similar to historical data (Fig. S7a, S7e). Discharge data at Q2 was mostly similar to prior data, but with an anomalously large pulse during the monsoon (Fig. S7c). To compare weathering dynamics against seasonal discharge, we constructed a synthetic hydrograph for the entire sampling transect during 2011 by combining data from the three different gauging stations. In other words, all samples are assumed to have the same relative changes in discharge with time such that the collection date can be used as a proxy for discharge. First, we normalized by the maximum flow of each year to calculate the daily fraction of maximum annual discharge. Then, these fractional terms from the three stations were aggregated into a single metric for the monthly fraction of averaged maximum annual discharge (Fig. S7), and it is this derived parameter against which we compare changes in chemical

weathering. We also consider a synthetic hydrograph constructed from historically averaged discharge, as opposed to only the discharge data of 2011, and find similar results (Fig. S7).

3. Results

3.1. Major ion chemistry

Ternary diagrams and timeseries of major ion concentrations and elemental ratios reveal both spatial and seasonal patterns (Fig. 2, 3). The ion Ca^{2+} is the dominant cation throughout the Langtang-Trisuli-Narayani River system and accounts for 46% to 79% of the sum of Ca^{2+} , Mg^{2+} , Na^+ , and K^+ , except for one sample at 25% (Fig. 2a). The cation Mg^{2+} is of secondary importance and accounts for 8% to 32% of Σ^+ . With the exception that both Na^+ and K^+ have a single outlier sample at 37%, Na^+ accounts for 5% to 22% of Σ^+ and K^+ accounts for 2% to 22% of Σ^+ . Overall, the major ion chemistry of the samples is consistent with prior observations (Harris et al., 1998; Galy & France-Lanord, 1999; Bhatt et al., 2009; Appendix 1). As found previously, samples from the Bhote Kosi and Trisuli Rivers are slightly enriched in Na^+ and K^+ relative to Ca^{2+} and Mg^{2+} when compared to samples from the greater Narayani River (Evans et al., 2004).

In the high-elevation sites, values of $(\text{Na}^++\text{K}^+)/\Sigma^+$ and Ca^{2+}/Σ^+ fall along a line of constant Mg^{2+}/Σ^+ near 10%. Conversely, differences among the lower-elevation stations LNS-1 to LNS-6 are predominantly between Ca^{2+}/Σ^+ and Mg^{2+}/Σ^+ with muted differences in $(\text{Na}^++\text{K}^+)/\Sigma^+$ around 10-20%. These observations are consistent with the high elevation sites weathering the Na^+ -rich and K^+ -rich HHC gneiss and schist, with lower elevation sites within the LH dominated by transitions between calcite and dolomite weathering. While the aggregate changes in $(\text{Na}^++\text{K}^+)/\Sigma^+$ are related to the site of sample collection, Na^+/Σ^+ and K^+/Σ^+ also exhibit strong trends related to the month

of sample collection (Fig. 2b). At a given value of $(\text{Ca}^{2+}+\text{Mg}^{2+})/\Sigma^+$, monsoon samples show a rotation to higher K^+/Σ^+ and lower Na^+/Σ^+ relative to samples from the non-monsoon.

The ratios $\text{Ca}^{2+}/\text{Na}^+$ and $\text{Ca}^{2+}/\text{Mg}^{2+}$ are elevated at most stations during the monsoon season (Fig. 3a, 3b). At LNS-4, however both ratios are highly variable. Because $[\text{K}^+]$ does not coherently decline during the monsoon season and $[\text{Na}^+]$ does decline during the monsoon, K^+/Na^+ is highest during the monsoon season at all stations. Likewise, monsoon K^+/Σ^+ is elevated at all stations (Fig. 3d). Thus, while $\text{Ca}^{2+}/\text{Na}^+$ is highest during the monsoon, the increase of $[\text{K}^+]$ relative to $[\text{Na}^+]$ and decline in absolute $[\text{Ca}^{2+}]$ and $[\text{Mg}^{2+}]$ results in muted seasonal change in Ca^{2+}/Σ^+ , although with Ca^{2+}/Σ^+ still generally higher during the monsoon season (Fig. 3c). Like $[\text{K}^+]$, $[\text{Cl}^-]$ is not always lower during the monsoon; the ratio Cl^-/Na^+ is highest during the monsoon, and Cl^-/Σ^+ is mostly weakly elevated during the monsoon (Fig. 3e). While Ca^{2+}/Σ^+ is still elevated during the monsoon relative to the non-monsoon seasons, some of this increase is associated with the weak increase in Cl^-/Σ^+ . That is, because Cl^-/Σ^+ increases during the monsoon, the relative supply of Ca^{2+} from precipitation also increases during the monsoon and partly decreases the Ca^{2+} attributed to lithologic weathering. Qualitatively, this observation suggests that we only weakly recover the monsoon increase in carbonate weathering fraction previously found in some datasets from Nepal (Tipper et al, 2006) and the Ganga-Brahmaputra basin (Sarin et al., 1989).

The dissolved anion budget in all of our samples is dominated by HCO_3^- , which comprises 49-84% of Σ^+ (the sum of conservative cations is equal to the sum of anions here because HCO_3^- is solved by charge balance) (Fig. 2c). The anion SO_4^{2-} typically represents 5% to 30% of the budget but rises as high as 49% in a subset of samples from in headwaters at the Lirung Glacier. The anion

Cl⁻ is typically 1% to 13% of the anion budget but reaches 20%-39% for the July and August sampling of LNS-4 and the August sampling of LNS-7 (Fig. 2d). Notably, these three samples are those where the inversion model either found only few solutions or was unable to find any solutions. The ratio of $\text{SO}_4^{2-}/\Sigma^+$ decreases at almost all stations during the monsoon season, with the lowest ratios found in July and August (Fig. 3f). These raw data suggest seasonality in the fraction of weathering driven by FeS_2 oxidation.

3.2. Spatial and seasonal variability of $\delta^{34}\text{S}_{\text{SO}_4}$

Values of $\delta^{34}\text{S}_{\text{SO}_4}$ range from -4.5‰ to 9.0‰ (Fig. 4a). Averaged annually, $\delta^{34}\text{S}_{\text{SO}_4}$ is 3.9‰ at station LNS-16 and increases to 6-7‰ moving downstream through LNS-9, LNS-8, and LNS-7. Conversely, LNS-6 on the Bhote Koshi has an average $\delta^{34}\text{S}_{\text{SO}_4}$ of -2.0‰. Station LNS-5, which is after the confluence of these two river systems, has an intermediate $\delta^{34}\text{S}_{\text{SO}_4}$ value of 0.0‰. The value of $\delta^{34}\text{S}_{\text{SO}_4}$ increases within the Trisuli River to reach 1-2‰ at stations LNS-4 and LNS-3, declines to -3.7‰ at LNS-2, and finally increases to -1.5‰ at LNS-1 (Fig. 4a). Overall, the range of measured $\delta^{34}\text{S}_{\text{SO}_4}$ is largely consistent with prior values from the Alakananda-Bhagirathi rivers (Chakrapani & Veizer, 2006) and the Indus River Basin (Karim & Veizer, 2000).

The largest trend in $\delta^{34}\text{S}_{\text{SO}_4}$ is that samples from stations LNS-1 through LNS-6 tend to be ³⁴S-depleted relative to samples from stations LNS-7 through LNS-16 (Fig. 4b). Annual variability in $\delta^{34}\text{S}_{\text{SO}_4}$ at a given site is muted relative to this larger spatial pattern. Stations LNS-4 and LNS-5 have the largest seasonal $\delta^{34}\text{S}_{\text{SO}_4}$ variability; this is consistent with their position directly downstream of the confluence of the Bhote Koshi and Langtang Rivers, as the relative contribution

of SO_4^{2-} from each upstream river likely varies seasonally. Additionally, variability in LNS-4 may be partially attributable to pollution from the urban center of Betrawati (Appendix 2).

Values of $\delta^{34}\text{S}_{\text{SO}_4}$ are negatively correlated with $[\text{SO}_4^{2-}]$ when viewed across the whole dataset (Fig. 4c). At sites LNS-3 through LNS-6, $\delta^{34}\text{S}_{\text{SO}_4}$ decreases seasonally with increasing $[\text{SO}_4^{2-}]$. For example, the May and September samples of LNS-5 with low $[\text{SO}_4^{2-}]$ have significantly higher $\delta^{34}\text{S}_{\text{SO}_4}$ values than samples with higher $[\text{SO}_4^{2-}]$. The non-linear decrease in $\delta^{34}\text{S}_{\text{SO}_4}$ with increasing $[\text{SO}_4^{2-}]$, at the scale of either individual stations or the entire data suite, ostensibly resembles a mixing curve with multiple $\%$ of scatter in $\delta^{34}\text{S}_{\text{SO}_4}$ at a given value of $[\text{SO}_4^{2-}]$. However, $\delta^{34}\text{S}_{\text{SO}_4}$ values are not clearly related to changes in $\text{Cl}^-/\text{SO}_4^{2-}$ (Fig. 4d) or other major ion ratios (Fig. S9). For example, while samples from LNS-5 have a wide range of $\delta^{34}\text{S}_{\text{SO}_4}$ values inversely related with $[\text{SO}_4^{2-}]$, they have only a narrow range of $\text{Cl}^-/\text{SO}_4^{2-}$ ratios (Fig. 4d). Likewise, the entire set of $\delta^{34}\text{S}_{\text{SO}_4}$ measurements from LNS-1 through LNS-6, although systematically lower than those from LNS-7 through LNS-16, are not distinct in $\text{Cl}^-/\text{SO}_4^{2-}$ (Fig. 4d). Values of $\delta^{34}\text{S}_{\text{SO}_4}$ at stations LNS-1, LNS-2, and LNS-7 through LNS-10 are invariant with seasonal shifts towards higher $[\text{SO}_4^{2-}]$ during the non-monsoon season (Fig. 4c) and also have little relationship with $\text{Cl}^-/\text{SO}_4^{2-}$ (Fig. 4d). The major ion chemistry of our samples thus precludes two-component mixing as an explanation for the trend of $\delta^{34}\text{S}_{\text{SO}_4}$ with $[\text{SO}_4^{2-}]$; as described below, the observations require multiple lithologic end-members with variable $\delta^{34}\text{S}$.

3.3. Results of principal component analysis

The PCA of Z-scored $[\text{Ca}^{2+}]$, $[\text{Mg}^{2+}]$, $[\text{Na}^+]$, $[\text{K}^+]$, $[\text{Cl}^-]$, $[\text{SO}_4^{2-}]$, and $\delta^{34}\text{S}_{\text{SO}_4}$ identifies that 3 components explain 95% of normalized variance. The first component (PC-1) explains 66.3% of

variance and relates positive changes among all dissolved ion concentrations with inverse changes in $\delta^{34}\text{S}_{\text{SO}_4}$ (Fig. 5a). PC-1 predominantly distinguishes samples by the site of collection, not by the season of collection (Fig. 5b), and thus indicates that lithology is the first-order control on dissolved ion chemistry (as found in other settings; e.g., Bluth & Kump, 1994). PC-1 also shows seasonal influences; at a given site, factor scores of PC-1 are generally higher in samples collected during the monsoon period and lower in samples collected in the non-monsoon (Fig. 5b). The second principal component (PC-2) explains 21% of the normalized variance and also shows both spatial and seasonal trends (Fig. 5c). These results indicate that seasonality exerts a secondary control on major ion chemistry along the Langtang-Trisuli-Narayani River system (Bhatt et al., 2018). Using cluster analysis, Pant et al. (2018) likewise showed that in river waters from the Narayani basin lithology exerts the dominant control on dissolved chemistry and seasonality exerts a secondary influence.

PC-2 also inversely relates $\delta^{34}\text{S}_{\text{SO}_4}$ with $[\text{SO}_4^{2-}]$. Unlike PC-1, PC-2 does not strongly relate changes in $\delta^{34}\text{S}_{\text{SO}_4}$ with changes in $[\text{Ca}^{2+}]$, $[\text{Mg}^{2+}]$, or $[\text{Na}^+]$, which are the major products of chemical weathering. This result indicates a mode of variability between $[\text{SO}_4^{2-}]$ and $\delta^{34}\text{S}_{\text{SO}_4}$ largely independent from shifts in weathering lithology. One qualitative explanation for this observation is a shift in the $\delta^{34}\text{S}$ and weatherability of an end-member providing SO_4^{2-} to solution. An alternative explanation is microbial sulfate reduction in either the river sediments or tributaries, which would remove SO_4^{2-} and increase $\delta^{34}\text{S}_{\text{SO}_4}$ (Turchyn et al., 2013).

The strongest relation in PC-2 is a positive correlation between $[\text{K}^+]$ and $[\text{Cl}^-]$. Monsoon samples from the Lirung Glacier outlet show systematically higher factor scores for PC-2 than samples

from the non-monsoon (Fig. 5c). Given that these samples are relatively distant from direct anthropogenic influences, the covariation of $[K^+]$ and $[Cl^-]$ may reflect a true weathering dynamic.

4. Discussion

4.1. Mixing relations require source of ^{34}S -depleted SO_4^{2-}

The high Ca^{2+}/Σ^+ and low Na^+/Σ^+ of samples from throughout the Langtang-Trisuli-Narayani River systems indicate that the majority of positive charge in solution derives from either the carbonate mineral or precipitation end-members (Fig. 6a). The contribution of rainwater to the dissolved ion budget is ultimately limited by $[Cl^-]$ (Fig. 6b). Given that the majority of cation charge must then be derived from calcite and dolomite weathering, the river water samples have significantly higher SO_4^{2-}/Σ^+ than can be explained without an additional source of SO_4^{2-} (Fig. 6c). Furthermore, the $\delta^{34}S_{SO_4}$ of the samples is significantly lower than the $\delta^{34}S$ values of calcite, dolomite, or precipitation (Fig. 6d). The elevated SO_4^{2-}/Σ^+ and low $\delta^{34}S_{SO_4}$ of samples thus requires an additional source of ^{34}S -depleted sulfur. As previously suggested for the Langtang River (Bhatt et al., 2000; 2018) and shown in the Marsyandi catchment (Turchyn et al., 2013; Hemingway et al., 2020), a likely source of this sulfur is the oxidation of FeS_2 . The oxidation of FeS_2 to H_2SO_4 and subsequent weathering of minerals could increase river SO_4^{2-}/Σ^+ and, depending on the value of $\delta^{34}S_{FeS_2}$, decrease $\delta^{34}S_{SO_4}$ to observed values (Fig. 6c, 6d, red boxes).

4.2. Sources of dissolved ions

Our inversion model finds that the contribution of each end-member to river chemistry varies by element, site, and season (Fig. 7; Fig. S10). Calcite sources the majority of Ca^{2+} in solution, while Mg^{2+} is sourced from both dolomite and silicate end-members. The importance of dolomite

weathering increase at the expense of calcite moving downstream (Fig. 7c, 7d). This shift reflects an increasing influence of LH lithologies, which include massive dolomites, as the river leaves the predominantly silicate mineralogy of HHC (Fig. 1). This observation again demonstrates the first-order control of site location on dissolved chemistry (Bluth & Kump, 1994), consistent with the result of the principal component analysis.

The silicate and biotite end-members dominate contributions to the budgets of Na^+ and K^+ . Seasonally, results indicate a strong monsoon increase in the weathering of biotite relative to the silicate end-member. One explanation for seasonal changes in biotite contribution is changing glacial weathering. Researchers have previously demonstrated that glacial weathering is typically enriched in K^+ and Ca^{2+} (Anderson et al., 1997; 2000). Following mechanical abrasion and the build-up of strain in biotite, K^+ release can occur through leaching or vermiculitization of the damaged mineral lattice. These processes may be exacerbated through either seasonal melting or higher subglacial discharge, explaining the higher biotite contribution during the monsoon. Because the monsoon increase in biotite weathering is reflected across all sample locations, an explanation from glacial weathering would require a significant contribution of meltwater to the lower Trisuli River. Indeed, ~10% of total discharge is attributable to meltwater (Andermann et al., 2012), suggesting that a seasonal signal of glacial weathering could explain the higher contributions of biotite during the monsoon season. The monsoonal increase in K^+/Σ^+ might alternatively reflect seasonal landslides and the exposure of freshly abraded surfaces (Emberson et al., 2017). Another explanation for the increase in K^+/Na^+ (Fig. 2b) could be a change in clay formation; a simultaneous release from clays of K^+ and Cl^- would explain both the shift towards biotite weathering and the strong covariation of K^+ with Cl^- (Fig. 3). Finally, leucogranites in the

Langtang valley have variable K^+/Na^+ ratios, and leucogranites generally show inverse abundances of K^+ and Na^+ (Inger & Harris, 1993). The shift from the silicate to biotite end-member that we see in our model results may represent a seasonal transition from weathering of the HHC gneiss to a high- K^+/Na^+ leucogranite.

4.3. Inversion-constrained fraction of FeS_2 -derived SO_4^{2-} and $\delta^{34}S_{FeS_2}$

The median fraction of FeS_2 -derived SO_4^{2-} ranges from 62% to 101% (Fig. 8a). These findings are consistent with the prior estimate that 70% of $[SO_4^{2-}]$ in this river system derives from FeS_2 oxidation (Galy & France-Lanord, 1999). If this FeS_2 -derived SO_4^{2-} had a single characteristic $\delta^{34}S$ across all of our samples, mass balance would result in a clear relationship between the measured $\delta^{34}S_{SO_4}$ and the fraction of total SO_4^{2-} attributed to FeS_2 oxidation (Fig. 8b). Specifically, an increase in the fraction of SO_4^{2-} attributed to FeS_2 oxidation should pull measured $\delta^{34}S_{SO_4}$ values towards the $\delta^{34}S$ of the FeS_2 end-member. In contrast, our inversion results do not recover a clear relationship between $\delta^{34}S_{SO_4}$ and the fraction of FeS_2 -derived SO_4^{2-} . For example, while station LNS-1 exhibits a range of chemical compositions indicating that 64% to 93% of SO_4^{2-} is derived from FeS_2 oxidation, measured $\delta^{34}S_{SO_4}$ remains nearly constant throughout the year at $-1.5 \pm 0.6\%$. This result emerges directly from our raw observations of a minimal relationship between $\delta^{34}S_{SO_4}$ and Cl^-/SO_4^{2-} (Fig. 4b).

Our results indicate that the $\delta^{34}S$ of FeS_2 -derived SO_4^{2-} is variable. Using the model-constrained fraction of FeS_2 -derived SO_4^{2-} , measured $\delta^{34}S_{SO_4}$, and a range of values of the $\delta^{34}S_{SO_4}$ of precipitation, we use mass balance to calculate the $\delta^{34}S$ of FeS_2 required by each sample. The uncertainty associated with each determination of $\delta^{34}S_{FeS_2}$ thus reflects the possible range in the

fraction of SO_4^{2-} derived from FeS_2 oxidation. Calculated $\delta^{34}\text{S}_{\text{FeS}_2}$ values fall broadly into two groups (Fig. 8c, 8d). At station LNS-7 through LNS-16, 80% of the data are explained with median $\delta^{34}\text{S}_{\text{FeS}_2}$ values of 1.7‰ to 6.2‰ (Fig. 8c). In contrast, 80% of the data from LNS-1 through LNS-6 are explained with median $\delta^{34}\text{S}_{\text{FeS}_2}$ values of -7.0‰ to 0.0‰ (Fig. 8c).

The two groups of samples with distinct $\delta^{34}\text{S}_{\text{FeS}_2}$ values reflect the larger lithological context of the Nepal Himalaya. The catchments of stations LNS-7 through LNS-16 (with 80% of calculated $\delta^{34}\text{S}_{\text{FeS}_2}$ values between 1.7‰ to 6.2‰) are entirely underlain by HHC, with no exposure of LH or TSS lithologies (Fig. 8d). The FeS_2 -derived SO_4^{2-} in the Langtang River is thus likely sourced principally from igneous or metamorphic sulfides in the metapelites and leucogranites of the HHC. FeS_2 has been observed as an accessory phase in Langtang rocks (Inger & Harris, 1992; 1993). The isotope composition of igneous sulfide minerals has previously been estimated to range from -10 to +10‰ (Thode, 1991; Karim & Veizer, 2000). Overall, the median $\delta^{34}\text{S}_{\text{FeS}_2}$ values are ^{34}S -enriched relative to bulk Earth and are similar to the average global river $\delta^{34}\text{S}_{\text{SO}_4}$ of approximately 4.5‰ (Macnamara & Thode, 1950; Burke et al., 2018).

Conversely, the catchments of stations LNS-1 through LNS-6 (with 80% of calculated $\delta^{34}\text{S}_{\text{FeS}_2}$ values between -7.0‰ to 0.0‰) contain substantial outcroppings of TSS and LH (Fig. 8d). As described above, the inversion-constrained values of $\delta^{34}\text{S}_{\text{FeS}_2}$ reflect the net $\delta^{34}\text{S}$ of SO_4^{2-} sourced from both sulfide mineral oxidation and S_{org} oxidation. Because organic matter in the TSS can influence $\delta^{34}\text{S}_{\text{FeS}_2}$, the shift in $\delta^{34}\text{S}_{\text{FeS}_2}$ relative to LNS-7 through LNS-16 may reflect either a change in the $\delta^{34}\text{S}$ of weathering sulfide minerals or possibly the oxidation of ^{34}S -depleted S_{org} that was not present in HHC bedrock. Because organic matter tends to have a molar $\text{C}_{\text{org}} : \text{S}_{\text{org}}$ ratio of

approximately 100:1, sourcing any significant fraction of dissolved $[\text{SO}_4^{2-}]$ from oxidation of organic matter entails a large flux of carbon. Attributing 100% of $[\text{HCO}_3^-]$ to organic matter oxidation at stations LNS-1 through LNS-6 would explain only 4% to 25% of $[\text{SO}_4^{2-}]$, indicating that most river SO_4^{2-} is not derived from S_{org} oxidation. Furthermore, major ion concentrations and prior measurements of DIC $\delta^{13}\text{C}$ (Galy & France-Lanord, 1999) both indicate that carbonate weathering is a significant source of HCO_3^- . While a contribution from S_{org} oxidation is still possible, it is more parsimonious to attribute the downstream shift in $\delta^{34}\text{S}_{\text{FeS}_2}$ to a change in the $\delta^{34}\text{S}$ of weathering sulfide minerals. Sedimentary pyrites tend to have low $\delta^{34}\text{S}$ values due to their formation by the fractionating process of microbial sulfate reduction (Thode et al., 1951; Sim et al., 2011), and could feasibly be ^{34}S -depleted relative to the sulfide minerals of the HHC. Previous work in the Marsyandi river has shown that SO_4^{2-} derived from FeS_2 oxidation in the TSS reaches $\delta^{34}\text{S}$ values as low as approximately -25‰, consistent with but lower than our minimum estimates of $\delta^{34}\text{S}_{\text{FeS}_2}$ in downstream stations (Turchyn et al., 2013; Hemingway et al., 2020).

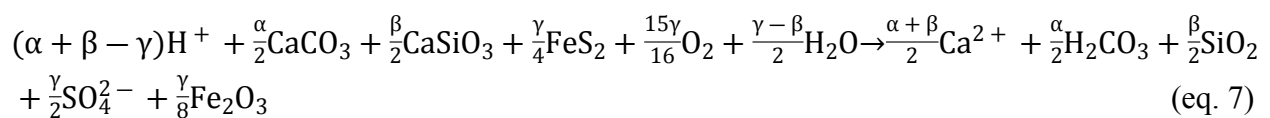
Our findings are similar to prior observations from the Indus River Basin where a decline in $\delta^{34}\text{S}_{\text{SO}_4}$ from headwater to lowland samples was likewise attributed to a transition from weathering igneous and metamorphic sulfide minerals to the weathering of sedimentary sulfides (Karim & Veizer, 2000). Similarly, our results are in agreement with findings that weathering of magmatic sulfides may impact dissolved chemistry in the Marsyandi River downstream of the TSS (Turchyn et al., 2013). However, our measurements emphasize the possibility that, as previously considered and refuted in Turchyn et al. (2013), a second FeS_2 end-member with relatively high $^{34}\text{S}/^{32}\text{S}$ ratio, or alternatively a range of end-members with variable $^{34}\text{S}/^{32}\text{S}$ ratios, may contribute to an observed rise in $\delta^{34}\text{S}_{\text{SO}_4}$ within the TSS section of the Marsyandi River.

4.4. Climatic implications of weathering in the Langtang-Trisuli-Narayani River system

The weathering of carbonate and silicate minerals by H_2CO_3 or H_2SO_4 have distinct impacts on the fluxes of ALK and DIC. After formalizing a framework introduced in Torres et al. (2016) we apply this methodology to show that weathering in the Langtang-Trisuli-Narayani River system is not a source or sink of CO_2 over timescales greater than carbonate compensation (5-10 Kyr) (Archer et al., 1997; 2000) and shorter than the marine SO_4^{2-} residence time (about 10 Myr).

4.4.1. Impacts of sulfuric acid weathering on ΔALK and ΔDIC

The chemical weathering of carbonate and silicate minerals can be described as titration reactions (eqs. 1 and 4) where the source of H^+ can be either H_2CO_3 or H_2SO_4 (eq. 5). Because reactions are written with each chemical species in the dominant form it would take at the CO_2 equivalence point, the ΔALK and ΔDIC of each equation are the stoichiometric factors on H^+ and H_2CO_3 , respectively (Zeebe & Wolf-Gladrow, 2001). Taking β and α to represent the production of ALK through silicate (eq. 1) and carbonate weathering (eq. 4), respectively, and γ the consumption of ALK through FeS_2 oxidation through reduction of O_2 (eq. 5), a generic weathering reaction is constructed from their weighted sum (eq. 7). This net reaction shows that $\Delta\text{ALK} = \alpha + \beta - \gamma$ and $\Delta\text{DIC} = \alpha/2$. Note that, unlike Torres et al. (2016), here we do not require the explicit coupling of H^+ production and H^+ consumption. Because α and β reflect the flux of ALK and not Ca^{2+} specifically, these formulations of ΔALK and ΔDIC are general across mineral stoichiometries.



The parameter R is defined as the ratio of carbonate weathering to total weathering (eq. 8) and is equal to $\frac{\alpha}{\alpha + \beta}$. The parameter Z is defined as the fraction of weathering done with H₂SO₄ (eq. 9) and is equal to $\frac{\gamma}{\alpha + \beta}$. The fraction of silicate weathering to total weathering is 1-R, and the fraction of CO₂-driven weathering is 1-Z. Following inversion, R and Z can be defined explicitly as the sum of elemental contributions from each of the four lithologic end-members (eqs. 8 and 9). Brackets in equations 8 and 9 indicate the concentration of the indicated element that can be attributed to the subscripted end-member, and factors convert concentrations to units of charge equivalents. The numerator of R is thus the sum of Ca²⁺ and Mg²⁺ contributions from calcite and from dolomite, and the numerator of Z is the sum of SO₄²⁻ contributions from each of the four non-precipitation end-members shown as the sum over the ith end-member. Lastly, the denominator of both R and Z is the sum of Ca²⁺, Mg²⁺, Na⁺, and K⁺ contributions from each of the 4 weathering end-members, also shown as a sum over the ith end-member.

$$R = \frac{\alpha}{\alpha + \beta} = \frac{(2 * [Ca^{2+}]_{calcite} + 2 * [Ca^{2+}]_{dolomite} + 2 * [Mg^{2+}]_{dolomite})}{\sum_{i=1}^4 (2 * [Ca^{2+}]_i + 2 * [Mg^{2+}]_i + [Na^+]_i + [K^+]_i)} \quad (\text{eq. 8})$$

$$Z = \frac{\gamma}{\alpha + \beta} = \frac{\sum_{i=1}^4 (2 * [SO_4^{2-}]_i)}{\sum_{i=1}^4 (2 * [Ca^{2+}]_i + 2 * [Mg^{2+}]_i + [Na^+]_i + [K^+]_i)}$$

(eq. 9)

The net $\Delta\text{ALK}/\Delta\text{DIC}$ due to a weathering system is a simple function of R and Z (eq. 10). When viewed instantaneously, any flux with $\Delta\text{ALK}/\Delta\text{DIC} > 1$ will sequester CO₂ into the ocean while fluxes with $\Delta\text{ALK}/\Delta\text{DIC} < 1$ will source CO₂ to the atmosphere. The boundary for this instantaneous CO₂ flux is $Z = 1 - R/2$. The influence of chemical fluxes over longer timescales

depends on the removal rate of individual ions from the global ocean-atmosphere system. Because the reduction of SO_4^{2-} in marine sediments consumes H^+ and counteracts the ALK flux of terrestrial FeS_2 oxidation, FeS_2 oxidation during weathering influences climate on timescales shorter than the ~ 10 Myr marine residence time of SO_4^{2-} . During a transient period of time in which sulfide oxidation increases pCO_2 , marine SO_4^{2-} concentrations increase in tandem (Torres et al., 2014; Rennie et al., 2018). Carbonate mineral burial ultimately removes most of the alkalinity supplied to the global ocean from rivers, so a second relevant timescale is that of carbonate compensation. Because carbonate mineral burial removes ALK and DIC in a 2:1 ratio, fluxes with $\Delta\text{ALK}/\Delta\text{DIC} < 2$ represent sources of CO_2 to the atmosphere on timescales longer than carbonate compensation but shorter than the marine SO_4^{2-} residence time. The boundary for this long timescale CO_2 flux is $Z=1-R$, which implies that fluxes with $1 < \Delta\text{ALK}/\Delta\text{DIC} < 2$ are short-term sinks of atmospheric CO_2 but long-term sources (Torres et al., 2016).

$$\frac{\Delta\text{ALK}}{\Delta\text{DIC}} = \frac{(\alpha + \beta - \gamma)}{\alpha/2} = 2\left(\frac{\alpha + \beta - \gamma}{\alpha + \beta}\right) = 2\left(\frac{1 - \frac{\gamma}{\alpha + \beta}}{\frac{\alpha}{\alpha + \beta}}\right) = 2\frac{(1-Z)}{R} \quad (\text{eq. 10})$$

4.4.2. R and Z in the Langtang-Trisuli-Narayani River system

Except for one low value of R and two samples without successful inversion results, the median fraction of cations sourced from carbonate end-members in our samples ranges between 60% and 86% (Fig. 9). These values are consistent with previous studies of the Langtang-Trisuli-Narayani River system (West et al., 2002; Tipper et al., 2006; Galy & France-Lanord, 1999). The median fraction of acid sourced from FeS_2 oxidation ranges from 10% to 55%, similar to values calculated for the Andean middle mountains and floodplain of southern Peru (Torres et al., 2016). Values of R and Z in the Langtang-Trisuli-Narayani River system exhibit both seasonal and spatial trends,

but overall the data scatter around the line $Z = 1-R$ (Fig. 9a, 9b, S11, S12). As discussed above, the line $Z=1-R$ corresponds to $\Delta\text{ALK}/\Delta\text{DIC}=2$ and defines the line across which chemical weathering has no implications for the carbon cycle on timescales less than approximately 10 Myr. Our data thus straddle the line between long-term sources and sinks of pCO_2 ; we conclude that, within uncertainty, sulfide oxidation in the Narayani catchment may completely compensate for the canonical pCO_2 drawdown of silicate weathering. However, the spatial and seasonal changes in R and Z do shift whether the instantaneous flux is a source or sink of CO_2 . Understanding the origin of this chemical variability is critical for characterizing how the global carbon cycle has responded to Himalayan weathering throughout the Cenozoic.

4.4.2.1. Spatial changes in R and Z

The inversion results indicate minimal spatial variation in the fraction of carbonate weathering (R) (Fig. 9c, S9). This lack of downstream variation is unexpected given the change in lithology from the silicate-dominated HHC to the dolomite-rich LH (Fig. 1, S13). The lack of clear trend may reflect the supersaturation of Himalayan waters with respect to calcite, such that any downstream change in the magnitude of carbonate weathering is obscured by secondary carbonate precipitation (Bickle et al., 2015). An alternative explanation is that enhanced carbonate weathering associated with the transition to a dolomite-rich lithology is compensated by enhanced weathering of silicates as the river moves into a warmer and wetter environment (West et al., 2002).

In contrast, the fraction of acid sourced through FeS_2 oxidation (Z) decreases downstream (Fig. 9d). The mean Z value of the Lirung Glacier sites is 35%, decreasing to 28% at LNS-7 and LNS-8 in the downstream Langtang, and reaching a mean value of 23% in the lowermost 4 sampling

sites. The downstream decrease in the fraction of sulfuric acid weathering reflects the transition from a mountainous, highly erosive regime to a flatter environment with limited access to primary FeS_2 from bedrock erosion. The highest values of Z are found in glacial catchments, consistent with prior observations from glacial rivers (Anderson et al., 2000; Emberson et al., 2017) and inversion of global data (Torres et al., 2017). This effect can be explained because glaciers generate enhanced mineral surface area and disproportionately express weathering reactions with rapid kinetics, such as sulfide oxidation and carbonate dissolution (Gabet et al., 2008; Tranter & Wadham, 2014; Torres et al., 2017). The net effect of the consistently elevated Z values for some of our sampling sites in the headwaters, e.g., in the upper Langtang valley, together with little difference in R , is that these locations lie within the R - Z space characterized by long-term CO_2 release, even though the Narayani system as a whole falls in the region where sources and sinks are approximately balanced.

4.4.2.2. Seasonal changes in R

Prior studies have identified an increase in the fraction of carbonate weathering during the monsoon season in several sites throughout the Narayani River system, including the Lirung Glacier outlet within the upper Langtang Valley (Bhatt et al., 2000; Tipper et al., 2006), four sites in the Marsyandi basin with detailed time series data (Tipper et al., 2006), a series of small TSS-draining tributaries in the Marsyandi catchment with paired April/May and September samplings (Tipper et al., 2006; Bickle et al., 2015), the Trisuli River sampled at Betrawati (equivalent to our site LNS-4; Galy & France-Lanord, 1999), and the greater Ganges rivers (Sarin et al., 1989). One explanation for the observed seasonal increase in the fraction of carbonate weathering is a

hydrological transition in which, during the monsoon season, flow paths with shorter residence times become relatively more important than during the non-monsoon season (Tipper et al., 2006).

Due to the rapid dissolution kinetics of carbonate mineral relative to the slow dissolution kinetics of silicate minerals, a parcel of water given longer time for water-rock interaction may accumulate a larger fraction of silicate-derived cations (Tipper et al., 2006). As a result, water sourced from deeper flow paths with a longer residence time can be expected to have a larger fraction of silicate-derived cations. As the monsoon seasons begins and the water table rises, the source of water in the river channel may become dominated by flow paths with shorter residence times, potentially at shallower depths, and may thus express a higher fraction of carbonate-derived cations. In turn, the fraction of carbonate weathering may decline as the monsoon season wanes and deeper flow-paths with longer residences times increase their fractional contribution to water in the river channel (Tipper et al., 2006). This hydrological explanation for seasonal changes in the carbonate weathering ratio relies on changes in the ratio of water sourced from shallow flow paths to total discharge; this ratio may increase or decrease even if the absolute quantity of water sourced from both shallow and deeper flow paths increases due to heavy monsoon precipitation, an elevated groundwater table, and an increase in hydraulic head.

Unlike prior work, our analysis does not recover clear seasonal changes in R (Fig. 9c, 9e); this finding is seen when model results are plotted for individual months against sampling location (Fig. 9c top, colored symbols), clustered into belonging to either the monsoon season or the non-monsoon season (Fig. 9c bottom, black and white symbols), or as a timeseries (Fig. 9e). Although we do not have discharge measurements at all stations, we consider the values of R for different

relative discharges using a synthetic hydrograph (Fig. S7). Opposite to expectations from prior findings, regressions of R against the synthetic discharge curve do not show consistently positive relationships (Fig. 10). Thus, when considering all of the major ion concentration measurements (Fig. 9c, 9e), we do not recover the monsoon increase in R reported in prior work (Sarin et al., 1989; Tipper et al., 2006) (Fig. S14).

Application of our inversion calculation to previously published datasets shows that the lack of seasonality in R is not simply a result of the modeling approach we use (Fig. S14): our inversion model recovers monsoon increases in R for samples of the Trisuli River at Betrawati reported in Galy & France-Lanord (1999) (Fig. S14a) and in the Lirung Glacier outflow data of Bhatt et al. (2000) (Fig. S14c). Conversely, we find only minimal seasonal changes in R for the time-series data of Tipper et al. (2006) from tributaries of the Marsyandi River. However, the evidence for seasonal changes in carbonate weathering reported in Tipper et al. (2006) is primarily based on observations of $\text{Si(OH)}_4/\text{Ca}^{2+}$ and $^{87}\text{Sr}/^{86}\text{Sr}$ ratios, neither of which are included in our inversion model (Fig. S14f). A second potential reason for this disagreement is that the Marsyandi catchment contains hot springs that may source significant Cl^- to the river, which are also not included in our primary inversion (Fig. S4, S16), and thus the contribution of precipitation to the dissolved load may be overstated in our treatment of data from Tipper et al. (2006).

If observations of $[\text{K}^+]$ and $[\text{Cl}^-]$ are removed from the inversion, we do recover a clear seasonal increase in the fraction of carbonate weathering, broadly similar to that seen in prior work (Appendix 4, Fig. S17). The key difference between our results and those reported previously is thus our observation of elevated K^+/Σ^+ during the monsoon season (Fig. 3d), which sustains the

silicate weathering contribution to the solute load. This relative invariance of $[K^+]$ during the monsoon season (i.e., lack of dilution as seen for other solutes including $[Ca^{2+}]$) has been not documented in prior studies from the Nepal Himalaya. One explanation for our observation that K^+ behavior differs from that found in previous work could be that the processes responsible for sourcing K^+ have strengthened with time, for example if preferential leaching from glacially-ground minerals has become more efficient as glaciers have retreated. Such a change in weathering dynamics might explain why samples collected in the 1990s and early 2000s did not capture the effect that we see in samples from 2011, with potentially important implications for how changes in glacial dynamics over decadal timescales affect solute chemistry. Alternatively, we recognize that our observations of elevated $[K^+]$ may be an experimental artifact of bottle washing or sample collection. Furthermore, we note that inclusion of hot springs in the inversion results in a monsoon decrease in carbonate weathering fraction, opposite to prior findings (Fig. S16), while inclusion of an evaporite end-member does not meaningfully change our results (Fig. S15). In all cases, further study is warranted on the seasonally changing solute chemistry in rivers fed by Himalayan glaciers.

4.4.2.3. Seasonal changes in Z

Seasonal shifts in Z are significantly more pronounced than those in R, with the Z value of a given location lower during the monsoon season than during the non-monsoon (Fig. 9f). This monsoon decline in the proportion of solutes from H_2SO_4 -driven weathering is seen in 13 out of 16 stations and has an absolute magnitude of 1% to 13%, corresponding to a 3% to 40% relative change in the fraction of weathering driven by sulfuric acid (Fig. 9d). This seasonal change in Z is larger in the TSS-influenced sites than in the HHC-influenced sites. One consequence of the observed

seasonality is that the fraction of H_2SO_4 -driven weathering declines with higher fractional discharge (Fig. 10).

Our results agree with those reported for the Trisuli River by Galy and France-Lanord (1999), who report a seasonal decline in the ratio of SO_4^{2-} from sulfide oxidation and evaporite dissolution relative to the sum of total SO_4^{2-} and HCO_3^- . Application of our inversion model to their data recovers a monsoon-season decrease in Z (Fig. S14b). A monsoonal decrease in Z is also recovered in data from the Lirung Glacier outlet reported by Bhatt et al. (2000) (Fig. S14d) and in the Chame and Nar Khola timeseries data from Tipper et al. (2006) (Fig. S14g). Explanations for seasonal changes in Z depend on the subsurface structure of chemical weathering fronts, which are themselves determined by the long-term interaction of tectonics and weathering. Without additional observations of the FeS_2 and CaCO_3 weathering profiles in our sampling catchments, at this time we can only hypothesize as to the relevant mechanisms driving the observed seasonal solute dynamics. Below, we briefly evaluate the consistency of our observations with different erosional scenarios.

When the residence time of a mineral in the weathering zone is short relative to the time required for weathering, insufficient time for complete dissolution prevents the development of a complete subsurface dissolution front (i.e., the zone where mineral abundances decline to zero; Brantley & Lebedeva, 2011). This regime, termed “kinetic limitation”, contrasts with “supply limitation” wherein sufficient time is available for weathering such that the mineral abundances decline to zero below the weathering zone surface. Holding all other factors equal, minerals will transition from supply limitation to kinetic limitation as the erosion rate increases owing to a faster transit

through the weathering zone (West, 2012). The exact crossover point between kinetic limitation and supply limitation varies between different minerals depending upon their reactivity and abundance in the weathering zone; a reasonable expectation is that reactive minerals will remain supply limited over a larger range of erosion rates than will less reactive minerals (Gu et al., 2020). Under supply limitation, the position of a subsurface dissolution front may still shoal with increasing erosion.

When the residence time of FeS_2 in the weathering zone is relatively long, there may be sufficient time for the development of a deep FeS_2 dissolution front (Fig. 11, purple FeS_2 front). In this case, shallow flow paths would have minimal access to FeS_2 while deeper flow paths could accumulate SO_4^{2-} through FeS_2 oxidation. During the higher discharge of the monsoon season, an increase in the fraction of river channel water derived from shallower flow paths above a deep FeS_2 weathering front would lead to a seasonal reduction in the Z value recorded by the river chemistry. That is, enhanced discharge would result in a lower observed fraction of weathering driven by H_2SO_4 , consistent with our observations (Fig. 9, 10). Although a deep FeS_2 weathering front is difficult to reconcile with the high erosion rates of the Himalaya, much of the weathering in rapidly-eroding mountain belts takes place in bedrock, as opposed to soil profiles, and with influences from groundwater (Andermann et al., 2012; West, 2012).

When erosion rates are very high, FeS_2 may remain supply limited while only being depleted in a thin near-surface zone (Fig. 11, blue FeS_2 front). Under this condition, where all flow paths would have access to FeS_2 , seasonal transitions in the source of water entering the river channel are unlikely to explain the observed seasonality in Z . In this case, an alternative explanation for

observed seasonality comes from considering the changing supply of CO_2 and O_2 to the weathering system. During periods of high precipitation, an enhanced flux of CO_2 and O_2 are supplied to the subsurface for potential consumption in weathering reactions. If the waters hosting such weathering reactions are rapidly exported into the channel, this seasonal supply of acids and oxidants could influence the observed values of R and Z . When a seasonal flux of oxidant does not reach the FeS_2 weathering front, the seasonal reduction in Z could be caused by an increase in H_2CO_3 -driven weathering (Winnick et al., 2017). Alternatively, if the FeS_2 front is shallow, seasonal increases in the supply ratio of CO_2/O_2 could induce depletions in Z ; such an increase could be due to the oxidation of organic carbon formed during the non-monsoon season, or through a seasonal decrease of net oxygenic photosynthesis. In these cases, the observed changes in Z would result from altering the chemistry of water in shallow flow paths rapidly exported to the river channel, as opposed to changing the relative contributions of water from different hydrologic regions.

4.4.4. Extension to geologic timescales

The tectonic and erosional dynamics of the weathering system impact how seasonal changes might be representative of climatic changes over longer timescales. When extrapolated beyond seasonal timescales, our observations of seasonal change in Z ostensibly could indicate a negative feedback between discharge and FeS_2 oxidation (Fig. 10). Climate models show that global warming is associated with a strengthened hydrologic cycle and location-specific changes in runoff (Otto-Bliesner, 1995). Thus, if the patterns we observe are representative of responses over long time-scales, then higher temperatures, forced by higher pCO_2 , could result in greater discharge, lower fractions of FeS_2 oxidation, and a more effective silicate weathering cycle. Preliminary

evidence for such a feedback can be found in the Cenozoic increase of dissolved marine $[\text{SO}_4^{2-}]$ during the corresponding decline in pCO_2 inferred from CaCO_3 $\delta^{18}\text{O}$ (Zachos et al., 2001; Horita et al., 2002; Torres et al. 2014). However, the feedback between discharge and H_2SO_4 -driven weathering relies on the supply of O_2 and CO_2 relative to the position of the water table and relative to the FeS_2 and CaCO_3 weathering fronts (Fig. 11). Although presumably stable on the decadal timescales of concentration-discharge observations, this weathering dynamic is likely to shift due to long-term changes in tectonics and climate (Godsey et al., 2009, 2019; Ibarra et al., 2016). For example, if we assume that erosion rates balance uplift rates over tectonic timescales, the long-term control of Himalayan sulfide oxidation is likely to be tectonic shortening rather than river discharge. Indeed, the interplay between seasonal weathering dynamics and discharge likely changed throughout the uplift of the Himalaya and the initiation and development of the seasonal monsoon.

4.5. Inversion of published river observations from the Nepal Himalaya

Prior datasets of dissolved river chemistry from throughout the Nepal Himalaya were inverted using the same model as applied to our samples from the Langtang-Trisuli-Narayani River system (Table 1). The analyzed data in this analysis come from the Langtang River (Bhatt et al., 2009), the Marsyandi catchment (Bickle et al., 2005; Tipper et al., 2006, Wolff-Boenisch et al., 2009; Turchyn et al., 2013), the Yamuna catchment (Dalai et al., 2002), the greater Narayani basin (Galy & France-Lanord, 1999; Pant et al., 2018), rivers of the Western Himalayan (English et al., 2000; Quade et al., 2003), and the Ganges floodplain rivers (Sarin et al., 1989; Bickle et al., 2018). Analogous to our samples from the Langtang-Trisuli-Narayani River system, the larger dataset

reveals that carbonate weathering sources the majority of cations to solution, and there is strong evidence of extensive weathering driven by H_2SO_4 (Fig. 12).

Overall, analysis of R and Z in the previously published data reveal a transition from weathering as CO_2 -neutral in the mountainous front of the Himalaya to weathering as a sink of CO_2 in the floodplain. Samples from prior study of the Langtang-Trisuli-Narayani River system are similar to those reported here and show that FeS_2 oxidation largely offsets CO_2 drawdown due to silicate weathering throughout the eastern Narayani catchment. In a few cases, similar to the Langtang headwaters in our study, mountainous sites are characterized by long-term CO_2 release. Conversely, samples from the Ganges floodplain (Sarin et al., 1989; Galy & France-Lanord, 1999; Bickle et al., 2018) and silicate-dominated catchments within the Himalayan range (Quade et al., 2003) show lower fractions of carbonate weathering and sulfuric acid weathering, consistent with previous work showing that silicate weathering occurs predominantly in the lowland hills and Himalayan floodplain (Galy & France-Lanord, 1999; West et al., 2002; Lupker et al., 2012; Bickle et al., 2018; Bhatt et al., 2018).

5. Conclusions

Here we report the major ion concentration and $\delta^{34}\text{S}_{\text{SO}_4}$ of water samples collected monthly during 2011 from 16 sites along the Langtang-Trisuli-Narayani River system in the Nepal Himalaya. We evaluate the role of lithology and seasonality in the supply and isotope composition of river SO_4^{2-} and account for the alkalinity flux from FeS_2 oxidation when evaluating the effect of Himalayan weathering on atmospheric pCO_2 over geologic time. Monte Carlo inversion modeling finds that, except for two samples, FeS_2 oxidation sources between 62% and 101% of dissolved SO_4^{2-} in our

samples. We find that $\delta^{34}\text{S}_{\text{SO}_4}$ principally reflects lithological $\delta^{34}\text{S}$ and is relatively constant at a given location throughout the sampled year. We recover spatial gradients in the magnitude of FeS_2 oxidation linked with weathering regime, as well as seasonal changes attributable to shifts in the relative importance of shallow and deep flow paths. Our results indicate that sulfide oxidation in the Narayani catchment may fully counteract the CO_2 drawdown associated with silicate weathering on timescales longer than carbonate compensation (5-10 Kyr) but shorter than the marine residence time of SO_4^{2-} (~10 Myr).

6. Data availability

The measurements of $\delta^{34}\text{S}_{\text{SO}_4}$ and dissolved major ion concentrations described in this article are available as supplementary materials.

7. Acknowledgements

P.C.K. is supported by the Fannie & John Hertz Foundation Cohan-Jacobs & Stein Families Fellowship. This research was conducted with government support under and awarded by DoD, Air Force Office of Scientific Research, National Defense Science and Engineering Graduate (NDSEG) Fellowship, 32 CFR 168a. N.F.D. is grateful to the Linde Center for support. The Environmental Analysis Center is supported by the Linde Center and the Beckman Institute at Caltech. This research was supported by the German Science Foundation DFG through the Cluster of Excellence 'CliSAP' (EXC177), Universität Hamburg. The authors acknowledge the Department of Hydrology and Meteorology (DHM), Government of Nepal, for discharge measurements. We thank the associate editor and three anonymous reviewers for their helpful

comments. The authors are grateful to W. Fischer for insightful conversations and to A. Philips and P. Mateo for advice on the design of figures.

8. Figure captions

Figure 1: Sampling locations and geologic map of the Langtang-Trisuli-Narayani River system. **(a)** The study region in central Nepal. **(b)** Elevation map with sample locations (white circles), labelled river network (blue), catchment boundaries (black), and geothermal springs (red triangles). Q1-Q3 indicate the locations of gauging stations (Fig. S7). Shaded oval indicates approximate location of samples described in Turchyn et al. (2013). Elevation color bar applies to **(b)** and **(c)** panels. **(c)** Elevation map at the confluence of the Langtang and Bhote Kosi rivers showing the relative positions of LNS-5 through LNS-9. **(d)** Geologic map of Nepal (Roback et al. (2018) after Dhital (2015)). Sample sites span the High Himalayan Crystalline and Lesser Himalayan sequences; although incompletely mapped, the Tethyn Sedimentary Series likely extends east into Tibet to be drained through the Bhote Kosi. Elevation data from the Shuttle Radar Topography Mission, locations of hot springs from Evans et al. (2008) and Becker et al. (2008).

Figure 2: Ternary diagrams for river water samples from the Langtang-Trisuli-Narayani River system show spatial and temporal gradients. Panels are color coded by either station number **(a, c)** or month of collection **(b, d)**, and are subsets of the full parameter space as indicated in the schematics (lower-left: filled white triangles are plotted areas, dashed triangles contain the full dataset, and grey triangles represent the full space). **(a)** The dominant cation in solution is Ca^{2+} . The cation Mg^{2+} is second in relative abundance, and $\text{Na}^+ + \text{K}^+$ represents a limited fraction of the charge budget. Spatial transitions between $(\text{Na}^+ + \text{K}^+)/\Sigma^+$ and Mg^{2+}/Σ^+ indicate the differing abundance of silicate and carbonate minerals in the HHC and LH. **(b)** The ratios Na^+/Σ^+ and K^+/Σ^+ shift seasonally in relative importance, with higher K^+/Na^+ ratio during the monsoon and lower ratio during the non-monsoon season. **(c)** The major anion in solution is HCO_3^- , except in the Lirung Glacier catchment where SO_4^{2-} occasionally has subequal contribution. **(d)** Monsoon season samples are occasionally significantly enriched in Cl^-/Σ^+ relative to samples from the non-monsoon season. All samples from this study are plotted in **(c)** and **(d)**. Plotted values reflect raw measurements without correction for inputs from precipitation. One sample with $(\text{Na}^+ + \text{K}^+)/\Sigma^+ \sim 60\%$ is out of the plotting range in **(a)**, and three samples are out of the plotting range in **(b)**.

Figure 3: Timeseries of dissolved ratios reported as the % variations from annual station means. **(a)** The cation ratio $\text{Ca}^{2+}/\text{Na}^+$ increases during the monsoon season relative to the non-monsoon. **(b)** The ratio $\text{Ca}^{2+}/\text{Mg}^{2+}$ also increases during the monsoon, consistent with a shift in either the relative fraction of silicate and carbonate weathering or a shift from dolomite to calcite weathering. **(c)** The ratio Ca^{2+}/Σ^+ tends to increase weakly during the monsoon. **(d)** The ratio K^+/Σ^+ increases

strongly during the monsoon. **(e)** The ratio Cl^-/Σ^+ shows a weak increase during the monsoon, which partially offsets the observed monsoon rise in Ca^{2+}/Σ^+ due to the high $\text{Ca}^{2+}/\text{Cl}^-$ of precipitation. **(f)** The ratio $\text{SO}_4^{2-}/\Sigma^+$ declines during the monsoon, suggesting a seasonal reduction in the fraction of weathering driven by sulfide oxidation. Note that each panel has a variable y-axis range, and that blue shading indicates the monsoon season.

Figure 4: Sample $\delta^{34}\text{S}_{\text{SO}_4}$, $[\text{SO}_4^{2-}]$, and $\text{Cl}^-/\text{SO}_4^{2-}$ coded by either **(a, c, d)** station number or **(b)** month of collection. **(a)** Mean station $\delta^{34}\text{S}_{\text{SO}_4}$ and annual range. Grey lines indicate confluences with major Narayani River tributaries. The catchments of stations LNS-7 through LNS-16 contain only HHC, while those of LNS-1 through LNS-6 contain TSS and LH as well. **(b)** Values of $\delta^{34}\text{S}_{\text{SO}_4}$ are typically higher at sites LNS-7 through LNS-16 than at sites LNS-1 through LNS-6. Values of $\delta^{34}\text{S}_{\text{SO}_4}$ are relatively constant throughout the year at a given station. **(c)** Values of $\delta^{34}\text{S}_{\text{SO}_4}$ against $[\text{SO}_4^{2-}]$. Across the sample suite, $\delta^{34}\text{S}_{\text{SO}_4}$ decreases downstream with increasing $[\text{SO}_4^{2-}]$, although this relationship only holds specifically for stations LNS-3 through LNS-6. **(d)** Values of $\delta^{34}\text{S}_{\text{SO}_4}$ against $\text{Cl}^-/\text{SO}_4^{2-}$. The lack of clear relationship argues against two-end member mixing as an explanation for the relation between $\delta^{34}\text{S}_{\text{SO}_4}$ and $[\text{SO}_4^{2-}]$. Error bars on $\delta^{34}\text{S}_{\text{SO}_4}$ and $[\text{SO}_4^{2-}]$ are 2σ .

Figure 5: **(a)** Biplot of principal component 1 (PC-1) and principal component 2 (PC-2). Labeled vectors indicate factor loadings, and symbols show the normalized factor scores of samples (Glover et al., 2011). Principal component 1 inversely relates $\delta^{34}\text{S}_{\text{SO}_4}$ with the concentration of all cations and anions. Principal component 2 inversely relates $[\text{SO}_4^{2-}]$ and $\delta^{34}\text{S}_{\text{SO}_4}$, and positively relates K^+ and Cl^- . **(b)** Sample factor scores of the first component, which captures the primary axis of variability in our chemical observations, principally varies by sampling site with a secondary seasonal influence. **(c)** Sample factor scores of the second component reflect seasonal variability, with larger seasonal changes in the Trisuli and Narayani Rivers than in the Langtang River.

Figure 6: Mixing diagrams color coded by **(a, c)** site location, or **(b, d)** month of collection. **(a)** The cross plot of Na^+/Σ^+ against Ca^{2+}/Σ^+ indicates that most cation charge is derived from carbonate minerals or precipitation, with a relatively small fraction derived from silicate weathering. **(b)** The cross plot of Na^+/Cl^- against $\text{Ca}^{2+}/\text{Cl}^-$ indicates mixing between a high- Cl^- end-member such as precipitation with the low- Cl^- of silicate and carbonate end-members. The contribution of precipitation is ultimately limited by sample $[\text{Cl}^-]$. The two samples not successfully inverted have low Na^+/Cl^- or $\text{Ca}^{2+}/\text{Cl}^-$ and are out of plotting range. **(c)** River samples show $\text{SO}_4^{2-}/\Sigma^+$ in excess of precipitation. The missing SO_4^{2-} can be provided through FeS_2 oxidation and subsequent weathering of carbonate and silicate minerals (red boxes), which sources both SO_4^{2-} and cations to solution. **(d)** Values of $\delta^{34}\text{S}_{\text{SO}_4}$ are lower than the rainwater or the carbonate end-members. The low $\delta^{34}\text{S}_{\text{SO}_4}$ values could be attained through FeS_2 oxidation (red box). For **(a)-(d)** grey boxes are centered around the mean of end-members distributions and extend 1σ . The red boxes define the mean and 1σ of end-members subject to H_2SO_4 weathering, although the $\delta^{34}\text{S}$ of those end-members is not prescribed during inversion. Although not used in the inversion, for illustrative purposes the $\delta^{34}\text{S}$ of calcite and dolomite are plotted as the range of Phanerozoic evaporites and the $\delta^{34}\text{S}$ of silicate and biotite are plotted as the value of terrestrial sulfur. Plotted $\delta^{34}\text{S}_{\text{SO}_4}$ errors are 2σ .

Figure 7: Median fractional contributions of end-members to (a) $[\text{Na}^+]$, (b) $[\text{K}^+]$, (c), $[\text{Ca}^{2+}]$, (d) $[\text{Mg}^{2+}]$, (e) $[\text{SO}_4^{2-}]$, and (f) $[\Sigma^+]$. Major trends include a downstream increase in the fraction of Mg^{2+} and SO_4^{2-} sourced from dolomite, as well as seasonal changes in the relative contribution of silicate and biotite to the Na^+ and K^+ budgets. Although the sum of median contributions is not constrained to equal 100%, in any individual simulation the sum of fractional contributions to each ion budget must fall between 85% and 115% of observations.

Figure 8: (a) FeS_2 -derived $\text{SO}_4^{2-}/\Sigma^+$ against observed $\text{SO}_4^{2-}/\Sigma^+$. Monte Carlo inversion finds that, except for two samples, a median value of 62%-101% of all dissolved SO_4^{2-} is derived from the oxidation of pyrite. (b) Measured $\delta^{34}\text{S}_{\text{SO}_4}$ and the fraction of FeS_2 -derived SO_4^{2-} . Any relationship between $\delta^{34}\text{S}_{\text{SO}_4}$ and the fraction of FeS_2 -derived SO_4^{2-} is weak. The inversion-constrained $\delta^{34}\text{S}_{\text{FeS}_2}$ value is calculated through mass balance and is conceptually very similar to the $\delta^{34}\text{S}$ value at 100% FeS_2 -derived SO_4^{2-} on a mixing line passing through both the sample and the precipitation end-member. (c) Inversion-constrained $\delta^{34}\text{S}_{\text{FeS}_2}$ against site location shows two distributions. The inversion recovers a ^{34}S -enriched population in samples draining the HHC and an ^{34}S -depleted population for samples with influence from the TSS and LH. (d) Inversion-constrained $\delta^{34}\text{S}_{\text{FeS}_2}$ against the catchment fraction of TSS and LH. A $\delta^{34}\text{S}_{\text{FeS}_2}$ of 0‰ largely separates the two sets of samples. Error bars for model output range from the 5th to 95th percentile of accepted simulation results.

Figure 9: (a,b) Fraction of weathering acid sourced from FeS_2 oxidation (Z) against the fraction of carbonate weathering (R), coded by either (a) sample site or (b) month of collection. Most data cluster around $Z=1-R$, the boundary between short-term and long-term CO_2 release. (c) R by site location and coded by season. Inversion results do not show clear spatial or seasonal changes. (d) Z arranged by site location and coded by season. Inversion results show a downstream decline in sulfuric acid weathering, and samples from the monsoon season have lower Z than those from the non-monsoon season. (e) Timeseries of variations in R relative to the annual station mean. R does not strongly covary with season. (f) Timeseries of variations in Z relative to the annual station mean. The value of Z is reduced during the monsoon at most sampling sites. Error bars for model output range from the 5th to 95th percentile of accepted simulation results.

Figure 10: Regression of R against the monthly fraction of maximum annual discharge shows positive and negative slopes, while regression of Z shows mostly negative slopes. Grey shading indicates the region with $dZ/dq < 0$. Error bars on dR/dq and dZ/dQ reflect the 5th to 95th percentile of Monte Carlo modeling for the regression slope of R or Z against a synthetic discharge curve (Fig. S7).

Figure 11: Schematic of seasonal weathering cycle with two possible positions for the CaCO_3 weathering front (orange, red) and FeS_2 weathering front (blue, purple). During all seasons O_2 and CO_2 reach the subsurface from both diffusive exchange with the atmosphere and advection of waters (Brantley et al., 2013). (a) Deep flow paths with long residence times accumulate SO_4^{2-} from FeS_2 oxidation and source water to the river channel during the non-monsoon. (b) During the monsoon, the ratio of water in the river channel sourced from shallow flow paths with shorter residence times may increase even as the absolute discharge through both shallow and deep flow paths increases. If the FeS_2 weathering front is deep (purple, lower erosion rates), a seasonal change in the contributions of flow paths with distinct residence times could cause lower Z values in river samples. If the FeS_2 weathering front is shallower (blue, higher erosion rates), a transition

in the hydrology of the system may not explain the observed seasonality of Z, which could instead reflect seasonal changes of the chemistry of water in flow paths with short residence times.

Figure 12: (a) Sample locations from prior publications reporting the dissolved chemistry of Himalayan rivers. Water chemistry is inverted and presented in subsequent panels even if detailed location data is unavailable. Latitude and longitude data for samples from Sarin et al. (1989) and Galy & France-Lanord (1999) were estimated using Google Earth. The two Western/Headwater samples that appear in the floodplain are Highland Rivers from Sarin et al. (1989). (b)-(e) Fraction of weathering acid sourced from FeS₂ oxidation (Z) against the fraction of carbonate weathering (R) grouped by location and coded by publication, showing data for both mainstem (closed symbols) and tributaries (open symbols). Shading indicates regions of $\Delta\text{ALK}/\Delta\text{DIC} < 1$, $1 < \Delta\text{ALK}/\Delta\text{DIC} < 2$, and $\Delta\text{ALK}/\Delta\text{DIC} > 2$, with different implications for pCO₂ drawdown over short and long timescales. (b) Langtang-Trisuli-Narayani River system samples tend to cluster around the line $Z = 1-R$, indicating that sulfide oxidation offsets much of the CO₂ drawdown associated with silicate weathering. (b) Marsyandi samples have high Z and high R values consistent with long-term CO₂ supply to the atmosphere. Samples draining the TSS are particularly high in Z (Turchyn et al., 2013). (c) Samples from the western headwaters of the Ganges and the Seti River are chemically similar to those from the Trisuli-Narayani catchment. (d) Samples from the floodplain have low Z and low R, indicative of silicate weathering driven predominantly with carbonic acid (Lupker et al., 2012; Bickle et al., 2018). Error bars for model output range from the 5th to 95th percentile of accepted simulation results.

9. Tables

Table 1: End-member means and uncertainty range

End-Member	Ca ²⁺ /Σ ⁺	Mg ²⁺ /Σ ⁺	Na ⁺ /Σ ⁺	K ⁺ /Σ ⁺	Cl ⁻ /Σ ⁺	SO ₄ ²⁻ /Σ ⁺
Precipitation	0.59 ± 0.20	0.13 ± 0.04	0.21 ± 0.18	0.07 ± 0.04	0.25 ± 0.23	0.17 ± 0.03
Silicate	0.15 ± 0.05	0.35 ± 0.10	0.40 ± 0.10	0.10 ± 0.10	0.00 ± 0.00	0.00 - 1.00
Biotite	0.15 ± 0.05	0.35 ± 0.10	0.10 ± 0.10	0.40 ± 0.10	0.00 ± 0.00	0.00 - 1.00
Calcite	1.00 ± 0.00	0.00 ± 0.00	0.00 ± 0.00	0.00 ± 0.00	0.00 ± 0.00	0.00 - 1.00
Dolomite	0.50 ± 0.10	0.50 ± 0.10	0.00 ± 0.00	0.00 ± 0.00	0.00 ± 0.00	0.00 - 1.00

10. References

- Andermann C., Bonnet S., & Gloaguen R. (2011). Evaluation of precipitation data sets along the Himalayan front. *Geochemistry, Geophysics, Geosystems*, **12**(7).
- Andermann C., Longuevergne L., Bonnet S., Crave A., Davy P., & Gloaguen R. (2012). Impact of transient groundwater storage on the discharge of Himalayan rivers. *Nature Geoscience*, **5**(2), 127.
- Anderson S., Drever J. I., & Humphrey N. F. (1997). Chemical weathering in glacial environments. *Geology*, **25**(5), 399-402.
- Anderson S. P., Drever J. I., Frost C. D., & Holden P. (2000). Chemical weathering in the foreland of a retreating glacier. *Geochimica et Cosmochimica Acta*, **64**(7), 1173-1189.
- Archer D., Kheshgi H., & Maier-Reimer E. (1997). Multiple timescales for neutralization of fossil fuel CO₂. *Geophysical Research Letters*, **24**(4), 405-408.
- Archer D., Winguth A., Lea D., & Mahowald N. (2000). What caused the glacial/interglacial atmospheric pCO₂ cycles?. *Reviews of Geophysics*, **38**(2), 159-189.

- Balci, N., Shanks III, W. C., Mayer, B., & Mandernack, K. W. (2007). Oxygen and sulfur isotope systematics of sulfate produced by bacterial and abiotic oxidation of pyrite. *Geochimica et Cosmochimica Acta*, **71**(15), 3796-3811.
- Balestrini R., Polesello S., & Sacchi E. (2014). Chemistry and isotopic composition of precipitation and surface waters in Khumbu valley (Nepal Himalaya): N dynamics of high elevation basins. *Science of the Total Environment*, **485**, 681-692.
- Beck R. A., Burbank D. W., Sercombe W. J., Riley G. W., Barndt J. K., Berry J. R., ... & Cheema A. (1995). Stratigraphic evidence for an early collision between northwest India and Asia. *Nature*, **373**(6509), 55.
- Becker J. A., Bickle M. J., Galy A., & Holland T. J. (2008). Himalayan metamorphic CO₂ fluxes: Quantitative constraints from hydrothermal springs. *Earth and Planetary Science Letters*, **265**(3-4), 616-629.
- Berner R. A. (1971). Worldwide sulfur pollution of rivers. *Journal of Geophysical Research*, **76**(27), 6597-6600.
- Berner R. A., & Caldeira K. (1997). The need for mass balance and feedback in the geochemical carbon cycle. *Geology*, **25**(10), 955-956.
- Bhatt M. P., Masuzawa T., Yamamoto M., Sakai A., & Fujita K. (2000). Seasonal changes in dissolved chemical composition and flux of meltwater draining from Lirung Glacier in the Nepal Himalayas. *IAHS Publication* **264**, 277-288.
- Bhatt M. P., Masuzawa T., Yamamoto M., & Gardner K. H. (2009). Spatial variations in chemical compositions along Langtang–Narayani river system in central Nepal. *Environmental geology*, **57**(3), 557-569.
- Bhatt M. P., Hartmann J., & Acevedo M. F. (2018). Seasonal variations of biogeochemical matter export along the Langtang-Narayani river system in central Himalaya. *Geochimica et Cosmochimica Acta*, **238**, 208-234.
- Bhattarai D. R. (1980). Some geothermal springs of Nepal. *Tectonophysics*, **62**(1-2), 7-11.
- Bickle M. J. (1996). Metamorphic decarbonation, silicate weathering and the long-term carbon cycle. *Terra Nova*, **8**(3), 270-276.
- Bickle M. J., Chapman H. J., Bunbury J., Harris N. B., Fairchild I. J., Ahmad T., & Pomiès C. (2005). Relative contributions of silicate and carbonate rocks to riverine Sr fluxes in the headwaters of the Ganges. *Geochimica et Cosmochimica Acta*, **69**(9), 2221-2240.
- Bickle M. J., Tipper E. D., Galy A., Chapman H., & Harris N. (2015). On discrimination between carbonate and silicate inputs to Himalayan rivers. *American Journal of Science*, **315**(2), 120-166.
- Bickle M. J., Chapman H. J., Tipper E., Galy A., Christina L., & Ahmad T. (2018). Chemical weathering outputs from the flood plain of the Ganga. *Geochimica et Cosmochimica Acta*, **225**, 146-175.
- Blum J. D., Gazis C. A., Jacobson A. D., & Chamberlain P. (1998). Carbonate versus silicate weathering in the Raikhot watershed within the High Himalayan Crystalline Series. *Geology*, **26**(5), 411-414.
- Bluth G. J., & Kump L. R. (1994). Lithologic and climatologic controls of river chemistry. *Geochimica et Cosmochimica Acta*, **58**(10), 2341-2359.
- Bordet P., Colchen M., Krummenacher D., Lefort P., Mouterde R., Remy M., 1971. Recherches Géologiques dans l'Himalaya du Nepal region de la Thakkhola. *Editions du centre national de la recherche scientifique*.

- Brantley S. L., & Lebedeva M. (2011). Learning to read the chemistry of regolith to understand the critical zone. *Annual Review of Earth and Planetary Sciences*, **39**, 387-416.
- Brantley S. L., Holleran M. E., Jin L., & Bazilevskaya E. (2013). Probing deep weathering in the Shale Hills Critical Zone Observatory, Pennsylvania (USA): the hypothesis of nested chemical reaction fronts in the subsurface. *Earth Surface Processes and Landforms*, **38(11)**, 1280-1298.
- Burke A., Present T. M., Paris G., Rae E. C., Sandilands B. H., Gaillardet J., ... & Voss B. M. (2018). Sulfur isotopes in rivers: Insights into global weathering budgets, pyrite oxidation, and the modern sulfur cycle. *Earth and Planetary Science Letters*, **496**, 168-177.
- Caldeira K. (1992). Enhanced Cenozoic chemical weathering and the subduction of pelagic carbonate. *Nature*, **357(6379)**, 578.
- Calmels D., Gaillardet J., Brenot A., & France-Lanord C. (2007). Sustained sulfide oxidation by physical erosion processes in the Mackenzie River basin: Climatic perspectives. *Geology*, **35(11)**, 1003-1006.
- Chakrapani G. J., & Veizer J. (2006). Source of dissolved sulphate in the Alakananda–Bhagirathi rivers in the Himalayas. *Current Science*, **90(4)**, 500-503.
- Claypool G. E., Holser W. T., Kaplan I. R., Sakai H., & Zak I. (1980). The age curves of sulfur and oxygen isotopes in marine sulfate and their mutual interpretation. *Chemical Geology*, **28**, 199-260.
- Collins R., & Jenkins A. (1996). The impact of agricultural land use on stream chemistry in the Middle Hills of the Himalayas, Nepal. *Journal of Hydrology*, **185(1-4)**, 71-86.
- Dalai T. K., Krishnaswami S., & Sarin M. M. (2002). Major ion chemistry in the headwaters of the Yamuna river system: Chemical weathering, its temperature dependence and CO₂ consumption in the Himalaya. *Geochimica et Cosmochimica Acta*, **66(19)**, 3397-3416.
- Dessert C., Dupré B., Gaillardet J., François L. M., & Allegre C. J. (2003). Basalt weathering laws and the impact of basalt weathering on the global carbon cycle. *Chemical Geology*, **202(3-4)**, 257-273.
- Dhital M. R. (2015). *Geology of the Nepal Himalaya: regional perspective of the classic collided orogen*. Springer.
- Edmond J. M. (1992). Himalayan tectonics, weathering processes, and the strontium isotope record in marine limestones. *Science*, **258(5088)**, 1594-1597.
- Elderfield H. (1986). Strontium isotope stratigraphy. *Palaeogeography, palaeoclimatology, palaeoecology*, **57(1)**, 71-90.
- Emberson R., Galy A., & Hovius N. (2017). Combined effect of carbonate and biotite dissolution in landslides biases silicate weathering proxies. *Geochimica et Cosmochimica Acta*, **213**, 418-434.
- English N. B., Quade J., DeCelles P. G., & Garzione C. N. (2000). Geologic control of Sr and major element chemistry in Himalayan Rivers, Nepal. *Geochimica et Cosmochimica Acta*, **64(15)**, 2549-2566.
- Evans M. J., Derry L. A., Anderson S. P., & France-Lanord C. (2001). Hydrothermal source of radiogenic Sr to Himalayan rivers. *Geology*, **29(9)**, 803-806.
- Evans M. J., Derry L. A., & France-Lanord C. (2004). Geothermal fluxes of alkalinity in the Narayani river system of central Nepal. *Geochemistry, Geophysics, Geosystems*, **5(8)**.
- Evans M. J., Derry L. A., & France-Lanord C. (2008). Degassing of metamorphic carbon dioxide from the Nepal Himalaya. *Geochemistry, Geophysics, Geosystems*, **9(4)**.

- Fort M. (1996). Late Cenozoic environmental changes and uplift on the northern side of the central Himalaya: a reappraisal from field data. *Palaeogeography, Palaeoclimatology, Palaeoecology*, **120(1-2)**, 123-145.
- France-Lanord C., & Derry L. A. (1997). Organic carbon burial forcing of the carbon cycle from Himalayan erosion. *Nature*, **390(6655)**, 65.
- François, L. M., & Walker, J. C. (1992). Modelling the Phanerozoic carbon cycle and climate: constraints from the $^{87}\text{Sr}/^{86}\text{Sr}$ isotopic ratio of seawater. *Am. J. Sci*, **292(2)**, 81-135.
- Gabet E. J., Burbank D. W., Pratt-Sitaula B., Putkonen J., & Bookhagen B. (2008). Modern erosion rates in the High Himalayas of Nepal. *Earth and Planetary Science Letters*, **267(3-4)**, 482-494.
- Gaillardet J., Dupré B., Louvat P., & Allegre C. J. (1999). Global silicate weathering and CO_2 consumption rates deduced from the chemistry of large rivers. *Chemical geology*, **159(1-4)**, 3-30.
- Galy A., & France-Lanord C. (1999). Weathering processes in the Ganges–Brahmaputra basin and the riverine alkalinity budget. *Chemical Geology*, **159(1-4)**, 31-60.
- Galy V., France-Lanord C., Beyssac O., Faure P., Kudrass H., & Palhol F. (2007). Efficient organic carbon burial in the Bengal fan sustained by the Himalayan erosional system. *Nature*, **450(7168)**, 407-410.
- Girault F., Bollinger L., Bhattarai M., Koirala B. P., France-Lanord C., Rajaure S., ... & Perrier F. (2014). Large-scale organization of carbon dioxide discharge in the Nepal Himalayas. *Geophysical Research Letters*, **41(18)**, 6358-6366.
- Glover, D. M., Jenkins, W. J., & Doney, S. C. (2011). Modeling methods for marine science. Cambridge University Press.
- Godsey S. E., Kirchner J. W., & Clow D. W. (2009). Concentration–discharge relationships reflect chemostatic characteristics of US catchments. *Hydrological Processes: An International Journal*, **23(13)**, 1844-1864.
- Godsey S. E., Hartmann J., & Kirchner J. W. (2019). Catchment chemostasis revisited: Water quality responds differently to variations in weather and climate. *Hydrological Processes*, **33(24)**, 3056-3069.
- Gu X., Rempe D. M., Dietrich W. E., West A. J., Lin T. C., Jin L., & Brantley S. L. (2020). Chemical reactions, porosity, and microfracturing in shale during weathering: The effect of erosion rate. *Geochimica et Cosmochimica Acta*, **269**, 63-100.
- Handa B.K. (1968). The chemical composition of rain water in some parts of North India. *Indian journal of meteorology & geophysics*, **19**, 175-180.
- Harris N., Bickle M., Chapman H., Fairchild I., & Bunbury J. (1998). The significance of Himalayan rivers for silicate weathering rates: evidence from the Bhote Kosi tributary. *Chemical Geology*, **144(3-4)**, 205-220.
- Hemingway J. D., Olson H., Turchyn A. V., Tipper E. T., Bickle M. J., & Johnston D. T. (2020). Triple oxygen isotope insight into terrestrial pyrite oxidation. *Proceedings of the National Academy of Sciences*.
- Hilton, R. G., Gaillardet, J., Calmels, D., & Birck, J. L. (2014). Geological respiration of a mountain belt revealed by the trace element rhenium. *Earth and Planetary Science Letters*, **403**, 27-36.
- Hilton, R. G., & West, A. J. (2020). Mountains, erosion and the carbon cycle. *Nature Reviews Earth & Environment*, **1(6)**, 284-299.

- Horita J., Zimmermann H., & Holland H. D. (2002). Chemical evolution of seawater during the Phanerozoic: Implications from the record of marine evaporites. *Geochimica et Cosmochimica Acta*, **66**(21), 3733-3756.
- Hren M. T., Chamberlain C. P., Hilley G. E., Blisniuk P. M., & Bookhagen B. (2007). Major ion chemistry of the Yarlung Tsangpo–Brahmaputra river: chemical weathering, erosion, and CO₂ consumption in the southern Tibetan plateau and eastern syntaxis of the Himalaya. *Geochimica et Cosmochimica Acta*, **71**(12), 2907-2935.
- Huh Y., Tsoi M. Y., Zaitsev A., & Edmond J. M. (1998). The fluvial geochemistry of the rivers of Eastern Siberia: I. Tributaries of the Lena River draining the sedimentary platform of the Siberian Craton. *Geochimica et cosmochimica acta*, **62**(10), 1657-1676.
- Ibarra D. E., Caves J. K., Moon S., Thomas D. L., Hartmann J., Chamberlain C. P., & Maher, K. (2016). Differential weathering of basaltic and granitic catchments from concentration–discharge relationships. *Geochimica et Cosmochimica Acta*, **190**, 265-293.
- Inger S., & Harris N. B. W. (1992). Tectonothermal evolution of the High Himalayan crystalline sequence, Langtang Valley, northern Nepal. *Journal of Metamorphic Geology*, **10**(3), 439-452.
- Inger S., & Harris N. (1993). Geochemical constraints on leucogranite magmatism in the Langtang Valley, Nepal Himalaya. *Journal of Petrology*, **34**(2), 345-368.
- Ivanov M. V., Grinenko V. A., & Rabinovich A. P. (1983). The sulphur cycle in continental reservoirs. *The Global Biogeochemical Sulphur Cycle–Scope*, **39**, 297-356.
- Jacobson A. D., Blum J. D., & Walter L. M. (2002). Reconciling the elemental and Sr isotope composition of Himalayan weathering fluxes: insights from the carbonate geochemistry of stream waters. *Geochimica et Cosmochimica Acta*, **66**(19), 3417-3429.
- John S. G., & Adkins J. F. (2010). Analysis of dissolved iron isotopes in seawater. *Marine Chemistry*, **119**(1-4), 65-76.
- Johnson J. E., Gerpheide A., Lamb M. P., & Fischer W. W. (2014). O₂ constraints from Paleoproterozoic detrital pyrite and uraninite. *Bulletin*, **126**(5-6), 813-830.
- Karim A., & Veizer J. (2000). Weathering processes in the Indus River Basin: implications from riverine carbon, sulfur, oxygen, and strontium isotopes. *Chemical Geology*, **170**(1-4), 153-177.
- Kerrick D. M., & Caldeira K. (1999). Was the Himalayan orogen a climatically significant coupled source and sink for atmospheric CO₂ during the Cenozoic?. *Earth and Planetary Science Letters*, **173**(3), 195-203.
- Krishnaswami S., & Singh S. K. (1998). Silicate and carbonate weathering in the drainage basins of the Ganga-Ghaghara-Indus head waters: Contributions to major ion and Sr isotope geochemistry. *Proceedings of the Indian Academy of Sciences-Earth and Planetary Sciences*, **107**(4), 283-291.
- Krishnaswami S., Singh S. K., and Dalai T. K. (1999) Silicate weathering in the Himalaya: Role in contributing to major ions and radiogenic Sr to the Bay of Bengal. In *Ocean Science, Trends and Future Directions* (ed. B. L. K. Somayajulu), pp. 23–51. India.
- Kump L. R., & Arthur M. A. (1997). Global chemical erosion during the Cenozoic: Weatherability balances the budgets. In *Tectonic uplift and climate change* (pp. 399-426). Springer, Boston, MA.
- Lerman A., Wu L., & Mackenzie F. T. (2007). CO₂ and H₂SO₄ consumption in weathering and material transport to the ocean, and their role in the global carbon balance. *Marine Chemistry*, **106**(1-2), 326-350.
- Li G., & Elderfield H. (2013). Evolution of carbon cycle over the past 100 million years. *Geochimica et Cosmochimica Acta*, **103**, 11-25.

- Lupker M., France-Lanord C., Galy V., Lavé J., Gaillardet J., Gajurel A. P., ... & Sinha R. (2012). Predominant floodplain over mountain weathering of Himalayan sediments (Ganga basin). *Geochimica et Cosmochimica Acta*, **84**, 410-432.
- Macnamara J., & Thode H. G. (1950). Comparison of the isotopic constitution of terrestrial and meteoritic sulfur. *Physical Review*, **78(3)**, 307.
- Maher, K., & Chamberlain, C. P. (2014). Hydrologic regulation of chemical weathering and the geologic carbon cycle. *Science*, 343(6178), 1502-1504.
- Millot R., Gaillardet J., Dupré B., & Allègre C. J. (2002). The global control of silicate weathering rates and the coupling with physical erosion: new insights from rivers of the Canadian Shield. *Earth and Planetary Science Letters*, **196(1-2)**, 83-98.
- Myrow, P. M., Hughes, N. C., Derry, L. A., McKenzie, N. R., Jiang, G., Webb, A. A. G., ... & Singh, B. P. (2015). Neogene marine isotopic evolution and the erosion of Lesser Himalayan strata: Implications for Cenozoic tectonic history. *Earth and Planetary Science Letters*, 417, 142-150.
- Négrel P., Allègre C. J., Dupré B., & Lewin E. (1993). Erosion sources determined by inversion of major and trace element ratios and strontium isotopic ratios in river water: the Congo Basin case. *Earth and Planetary Science Letters*, **120(1-2)**, 59-76.
- Otto-Bliesner B. L. (1995). Continental drift, runoff, and weathering feedbacks: Implications from climate model experiments. *Journal of Geophysical Research: Atmospheres*, **100(D6)**, 11537-11548.
- Pant R. R., Zhang F., Rehman F. U., Wang G., Ye, M., Zeng C., & Tang H. (2018). Spatiotemporal variations of hydrogeochemistry and its controlling factors in the Gandaki River Basin, Central Himalaya Nepal. *Science of the Total Environment*, **622**, 770-782.
- Panthi J., Dahal P., Shrestha M., Aryal S., Krakauer N., Pradhanang, S., ... & Karki R. (2015). Spatial and temporal variability of rainfall in the Gandaki River Basin of Nepal Himalaya. *Climate*, **3(1)**, 210-226.
- Paris G., Sessions A. L., Subhas A. V., & Adkins J. F. (2013). MC-ICP-MS measurement of $\delta^{34}\text{S}$ and $\Delta^{33}\text{S}$ in small amounts of dissolved sulfate. *Chemical Geology*, **345**, 50-61.
- Pierson-Wickmann A. C., Reisberg L., & France-Lanord C. (2000). The Os isotopic composition of Himalayan river bedloads and bedrocks: importance of black shales. *Earth and Planetary Science Letters*, **176(2)**, 203-218.
- Quade J., English N., & DeCelles P. G. (2003). Silicate versus carbonate weathering in the Himalaya: a comparison of the Arun and Seti River watersheds. *Chemical Geology*, **202(3-4)**, 275-296.
- Quay P. D., Wilbur D. O., Richey J. E., Devol A. H., Benner R., & Forsberg B. R. (1995). The $^{18}\text{O}:^{16}\text{O}$ of dissolved oxygen in rivers and lakes in the Amazon Basin: determining the ratio of respiration to photosynthesis rates in freshwaters. *Limnology and Oceanography*, **40(4)**, 718-729.
- Rabinovich A. L., & Grinenko V. A. (1979). Sulfate sulfur isotope ratios for USSR river water. *Geochemistry International*, **16**, 68-79.
- Raymo M. E., Ruddiman W. F., & Froelich P. N. (1988). Influence of late Cenozoic mountain building on ocean geochemical cycles. *Geology*, **16(7)**, 649-653.
- Raymo M. E., & Ruddiman W. F. (1992). Tectonic forcing of late Cenozoic climate. *Nature*, **359(6391)**, 117.
- Raymo M. I. (1994). The Himalayas, organic carbon burial, and climate in the Miocene. *Paleoceanography and Paleoclimatology*, **9(3)**, 399-404.

- Raymond, P. A., Hartmann, J., Lauerwald, R., Sobek, S., McDonald, C., Hoover, M., ... & Kortelainen, P. (2013). Global carbon dioxide emissions from inland waters. *Nature*, 503(7476), 355-359.
- Rennie V. C., Paris G., Sessions A. L., Abramovich S., Turchyn A. V., & Adkins J. F. (2018). Cenozoic record of $\delta^{34}\text{S}$ in foraminiferal calcite implies an early Eocene shift to deep-ocean sulfide burial. *Nature Geoscience*, **11**(10), 761.
- Riebe C. S., Kirchner J. W., Granger D. E., & Finkel R. C. (2001). Strong tectonic and weak climatic control of long-term chemical weathering rates. *Geology*, **29**(6), 511-514.
- Roback K., Clark M. K., West A. J., Zekkos D., Li G., Gallen S. F., ... & Godt J. W. (2018). The size, distribution, and mobility of landslides caused by the 2015 Mw7. 8 Gorkha earthquake, Nepal. *Geomorphology*, **301**, 121-138.
- Sarin M. M., & Krishnaswami S. (1984). Major ion chemistry of the Ganga–Brahmaputra river systems, India. *Nature*, **312**(5994), 538.
- Sarin M. M., Krishnaswami S., Dilli K., Somayajulu B. L. K., & Moore W. S. (1989). Major ion chemistry of the Ganga-Brahmaputra river system: Weathering processes and fluxes to the Bay of Bengal. *Geochimica et cosmochimica acta*, **53**(5), 997-1009.
- Sarmiento J. L., & Gruber, N. (2006). Ocean biogeochemical dynamics. Princeton University Press.
- Sequeira R., & Kelkar D. (1978). Geochemical implications of summer monsoonal rainwater composition over India. *Journal of Applied Meteorology*, **17**(9), 1390-1396.
- Shrestha A. B., Wake C. P., Dibb J. E., & Whitlow S. I. (2002). Aerosol and precipitation chemistry at a remote Himalayan site in Nepal. *Aerosol Science and technology*, **36**(4), 441-456.
- Sim M. S., Bosak T., & Ono S. (2011). Large sulfur isotope fractionation does not require disproportionation. *Science*, **333**(6038), 74-77.
- Singh S. P., & Singh B. P. (2010). Geothermal evolution of the evaporite-bearing sequences of the Lesser Himalaya, India. *International Journal of Earth Sciences*, **99**(1), 101-108.
- Spence J., & Telmer K. (2005). The role of sulfur in chemical weathering and atmospheric CO₂ fluxes: evidence from major ions, $\delta^{13}\text{C}_{\text{DIC}}$, and $\delta^{34}\text{S}_{\text{SO}_4}$ in rivers of the Canadian Cordillera. *Geochimica et Cosmochimica Acta*, **69**(23), 5441-5458.
- Stallard R. F., & Edmond J. M. (1983). Geochemistry of the Amazon: 2. The influence of geology and weathering environment on the dissolved load. *Journal of Geophysical Research: Oceans*, **88**(C14), 9671-9688.
- Striegl R. G., Dornblaser M. M., McDonald C. P., Rover J. R., & Stets E. G. (2012). Carbon dioxide and methane emissions from the Yukon River system. *Global Biogeochemical Cycles*, **26**(4).
- Sundquist E. T. (1991). Steady-and non-steady-state carbonate-silicate controls on atmospheric CO₂. *Quaternary Science Reviews*, **10**(2-3), 283-296.
- Tipper E. T., Bickle M. J., Galy A., West A. J., Pomiès C., & Chapman H. J. (2006). The short term climatic sensitivity of carbonate and silicate weathering fluxes: insight from seasonal variations in river chemistry. *Geochimica et Cosmochimica Acta*, **70**(11), 2737-2754.
- Tipper E. T., Galy A., & Bickle M. J. (2008). Calcium and magnesium isotope systematics in rivers draining the Himalaya-Tibetan-Plateau region: Lithological or fractionation control?. *Geochimica et Cosmochimica Acta*, **72**(4), 1057-1075.
- Thode, H. G., Kleerekoper, H., & McElcheran, D. (1951). Isotope fractionation in the bacterial reduction of sulphate. *Research*, 4(12), 581.

- Thode, H. G. (1991). Sulphur isotopes in nature and the environment: an overview. *Stable isotopes: natural and anthropogenic sulphur in the environment*, 43, 1-26.
- Torres M. A., West A. J., & Li G. (2014). Sulphide oxidation and carbonate dissolution as a source of CO₂ over geological timescales. *Nature*, **507(7492)**, 346.
- Torres M. A., West A. J., Clark K. E., Paris G., Bouchez J., Ponton C., ... & Adkins J. F. (2016). The acid and alkalinity budgets of weathering in the Andes–Amazon system: Insights into the erosional control of global biogeochemical cycles. *Earth and Planetary Science Letters*, **450**, 381-391.
- Torres M. A., Moosdorf N., Hartmann J., Adkins J. F., & West A. J. (2017). Glacial weathering, sulfide oxidation, and global carbon cycle feedbacks. *Proceedings of the National Academy of Sciences*, **114(33)**, 8716-8721.
- Tranter M., & Wadham J. L. (2014). Geochemical weathering in glacial and proglacial environments. Treatise on geochemistry 2nd edition, *Surface and Ground Water, Weathering and Soils*, eds. Holland HD, Turekian KK (Elsevier).
- Tripathee L., Kang S., Huang J., Sharma C. M., Sillanpää M., Guo J., & Paudyal R. (2014). Concentrations of trace elements in wet deposition over the central Himalayas, Nepal. *Atmospheric environment*, **95**, 231-238.
- Tshering L. D., & Bhandari A. N. (1973). Geological report on the Salt Occurrences of Mustang area. Ministry of Industry & Commerce, Nepal Geological Survey.
- Turchyn A. V., Tipper E. T., Galy A., Lo J. K., & Bickle M. J. (2013). Isotope evidence for secondary sulfide precipitation along the Marsyandi River, Nepal, Himalayas. *Earth and Planetary Science Letters*, **374**, 36-46.
- Urey H. C. (1952). On the early chemical history of the earth and the origin of life. *Proceedings of the National Academy of Sciences of the United States of America*, **38(4)**, 351.
- Valdiya K.S. (1980) Geology of the Kumaun Lesser Himalayas. Wadia Institute of the Himalayan Geology, Dehra Dun, India.
- Veizer J. (1989). Strontium isotopes in seawater through time. *Annual Review of Earth and Planetary Sciences*, **17(1)**, 141-167.
- Walker J. C., Hays P. B., & Kasting J. F. (1981). A negative feedback mechanism for the long-term stabilization of Earth's surface temperature. *Journal of Geophysical Research: Oceans*, **86(C10)**, 9776-9782.
- West A. J., Bickle M. J., Collins R., & Brasington J. (2002). Small-catchment perspective on Himalayan weathering fluxes. *Geology*, **30(4)**, 355-358.
- West A. J., Galy A., & Bickle M. (2005). Tectonic and climatic controls on silicate weathering. *Earth and Planetary Science Letters*, **235(1-2)**, 211-228.
- West A. J. (2012). Thickness of the chemical weathering zone and implications for erosional and climatic drivers of weathering and for carbon-cycle feedbacks. *Geology*, **40(9)**, 811-814.
- White A. F., & Blum A. E. (1995). Effects of climate on chemical weathering in watersheds. *Geochimica et Cosmochimica Acta*, **59(9)**, 1729-1747.
- Winnick M. J., Carroll R. W., Williams K. H., Maxwell R. M., Dong W., & Maher K. (2017). Snowmelt controls on concentration-discharge relationships and the balance of oxidative and acid-base weathering fluxes in an alpine catchment, East River, Colorado. *Water Resources Research*, **53(3)**, 2507-2523.
- Wolff-Boenisch D., Gabet E. J., Burbank D. W., Langner H., & Putkonen J. (2009). Spatial variations in chemical weathering and CO₂ consumption in Nepalese High Himalayan

catchments during the monsoon season. *Geochimica et Cosmochimica Acta*, **73(11)**, 3148-3170.

Zachos J., Pagani M., Sloan L., Thomas E., & Billups K. (2001). Trends, rhythms, and aberrations in global climate 65 Ma to present. *Science*, **292(5517)**, 686-693.

Zeebe R. E., & Wolf-Gladrow D. (2001). CO₂ in seawater: equilibrium, kinetics, isotopes (No. 65). Gulf Professional Publishing.

Journal Pre-proofs

Declaration of interests

The authors declare that they have no known competing financial interests or personal relationships that could have appeared to influence the work reported in this paper.

The authors declare the following financial interests/personal relationships which may be considered as potential competing interests:

Journal Pre-proofs